# Mixing and Evaporation of Liquid Droplets Injected into an Air Stream Flowing at all Speeds

F. Moukalled\* and M. Darwish American University of Beirut Faculty of Engineering & Architecture Mechanical Engineering Department Riad El-Solh, 1107 2020 Beirut, Lebanon

#### **ABSTRACT**

This paper deals with the formulation, implementation, and testing of three numerical techniques based on (i) a full multiphase approach, (ii) a MUlti-SIze Group (MUSIG) approach, and (iii) a Heterogeneous MUSIG (H-MUSIG) approach for the prediction of mixing and evaporation of liquid droplets injected into a stream of air. The numerical procedures are formulated following an Eulerian approach, within a pressure-based fully conservative Finite Volume method equally applicable in the subsonic, transonic, and supersonic regimes, for the discrete and continuous phases. The k-ε two-equation turbulence model is used to account for the droplet and gas turbulence with modifications to account for compressibility at high speeds. The performances of the various methods are compared by solving for two configurations involving stream-wise and cross-stream spraying into subsonic and supersonic streams. Results, displayed in the form of droplet velocity vectors, contour plots, and axial profiles indicate that solutions obtained by the various techniques exhibit similar behavior. Differences in values are relatively small with the largest being associated with droplet volume fractions and vapor mass fraction in the gas phase. This is attributed to the fact that with MUSIG and H-MUSIG no droplet diameter equation is solved and the diameter of the various droplet phases are held constant, as opposed to the full multiphase approach.

# **Nomenclature**

 $A_p^{(k)}$ ,... coefficients in the discretized equation for  $\phi^{(k)}$ .

 $\mathcal{B}_{p}^{(k)}$  source term in the discretized equation for  $\phi^{(k)}$ .

 $B_{ij}$  breakup rate.

 $B'_{ii}$  breakup frequency.

 $C_{\rho}^{(k)}$  coefficient equals to  $1/R^{(k)}T^{(k)}$ .

 $C_D$  drag coefficient.

 $c_P$  specific heat at constant pressure.

 $C_{ii}$  coalescence rate.

d droplet diameter.

 $d_s$  Sauter diameter.

 $\mathbf{D}_{P}^{(k)}[\phi^{(k)}]$  the Matrix **D** operator.

f population fraction.

 $\mathbf{F}^{B}$  Body force.

 $\mathbf{F}^D$  drag force.

h static enthalpy.

 $h_{correction}$  correction coefficient for heat transport in droplet evaporation model.

 $H_{\rm P}[\phi^{(k)}]$  the H operator.

 $\mathbf{H}_{p}[\mathbf{u}^{(k)}]$  the vector form of the H operator.

k turbulence kinetic energy.

 $m_{correction}$  correction coefficient for mass transport in droplet evaporation model.

 $\dot{m}_d$  mass rate of droplet evaporation.

 $\dot{M}_d$  volumetric mass rate of droplet evaporation.

*n* number density distribution function.

 $P_k$  production term in k and  $\varepsilon$  equations.

*p* pressure.

Pr laminar Prandtl number of fluid/phase k.

Pr<sub>turb</sub> turbulent Prandtl number of fluid/phase k.

 $\dot{q}$  heat flux.

 $Q_{(k)}$  general source term of fluid/phase k.

 $R_{(k)}$  gas constant for fluid/phase k.

Re<sub>d</sub> Reynolds number based on the droplet diameter.

S source term.

 $\mathbf{S}_{\mathrm{f}}$  surface vector.

Sc Schmidt Number.

t time.

T temperature of fluid/phase k.

 $U_f$  interface flux velocity  $(\mathbf{v}_f^{(k)} \mathbf{S}_f)$ .

**u** velocity vector.

u,v velocity components in x- and y-direction, respectively.

 $X_{iki}$  mass fraction due to coalescence between groups j and k, which goes into

group i.

Y vapor mass fraction.

## **GREEK SYMBOLS**

 $\alpha$  volume fraction.

 $\varepsilon$  Turbulence dissipation rate.

 $\beta_{(k)}$  thermal expansion coefficient for phase/fluid k.

 $\eta$  Kolmogorov micro-scale.

 $\delta t$  time step.

 $\rho$  density.

au the stress tensor.

 $\lambda$  conductivity coefficient.

 $\lambda_c$  coalescence efficiency.

 $\omega_c$  collision frequency.

 $\Gamma$  diffusion coefficient.

 $\phi$  general scalar quantity.

 $\Delta h_{v}$  latent heat.

 $\mu,\mu_{turb},\mu_{eff}$  laminar, turbulent and effective viscosity of fluid/phase k.

 $\Omega$  cell volume.

# **SUBSCRIPTS**

d refers to the droplet discrete liquid phase.

eff refers to effective values.

f refers to interface.

g refers to the gas phase.

*i* refers to size group i.

*k* refers to phase k.

*nb* refers to the east, west, ... face of a control volume.

*NB* refers to the East, West, ... neighbors of the main grid point.

P refers to the P grid point.

s refers to the droplet surface condition.

sat refers to the saturation condition.

vap,g refers to the vapor specie in the gas phase.

#### INTRODUCTION

Recently there has been a revived interest in the injection of liquids in supersonic streams, particularly with respect to fuel injection techniques for hypersonic flights. These designs require air-breathing engines capable of supersonic combustion. Progress in the design of such engines depends among other things on the development of numerical tools for the simulation of its supersonic combustion process and related phenomena [1]. The following three key issues govern the performance of the liquid injection process in hypersonic engines: (i) the penetration of the fuel into the free-stream, (ii) the atomization of the injected fuel drops, and (iii) the level of fuel/air mixing [2]. It is important for the fuel to penetrate effectively into the free-stream so that the combustion process produces an even temperature distribution otherwise it will mostly occur along the surface of the combustor, causing inefficient combustor operation and increased cooling problems. Rapid atomization of the fuel is also required for efficient combustion. Increased atomization of the liquid fuel results in increased fuel/air mixing which allows a higher percentage of the fuel to be burnt in the short time before the entire mixture passes out of the combustor (generally the flow residence time is of the order of few milliseconds [3]). This paper is aimed at developing three numerical methods capable of predicting the spreading and evaporation of liquid droplets injected in gases flowing at all speeds.

The complex multi-phase flow phenomenon governing liquid injection applications involves a continuous gas phase usually composed of air and the evaporating vapor species from the fuel and one or more dispersed liquid phases. Approaches for the simulation of droplet transport and evaporation in combustion systems can be classified under two categories, namely the Lagrangian and Eulerian methods. Within both methods the gaseous phase is

calculated by solving the Navier-Stokes equations with a standard discretization method such as the Finite Volume Method.

In the **Lagrangian** approach [4,5,6], the spray is represented by discrete droplets which are advected explicitly through the computational domain while accounting for evaporation and other phenomena. Due to the large number of droplets in a spray, each discrete computational droplet is made to represent a number of physical droplets averaging their characteristics. The equations of motion of each droplet are a set of ordinary differential equations (ODE) which are solved using an ODE solver, a numerical procedure different from that of the continuous phase. To account for the interaction between the gaseous phase and the spray, several iterations of alternating solutions of the gaseous phase and the spray have to be conducted. Moreover, for turbulent flow simulation the above model has to be augmented with a stochastic or Monte-Carlo approach.

In the **Eulerian** approach [5,6,7,8], the evaporating spray is treated as an interacting and interpenetrating continuum, in analogy to the continuum approach of single phase flows, with each phase being described by a set of transport equations for mass, momentum and energy extended by interphase exchange terms. This description allows the gaseous phase and the spray to be discretized by the same method, and therefore to be solved by the same numerical procedure. Because of the presence of multiple phases a multiphase algorithm is used rather than a single-phase one.

The widely used Lagrangian approach has been shown to be efficient in several situations. Its main shortcomings, however, are the limited possibility for parallelization as a result of the coupling to an Eulerian description of the gaseous phase, and the large memory and CPU requirements dictated by the numerous number of parcels needed in each control volume of the computational domain for accurate predictions. These disadvantages make the use of an Eulerian approach a desirable alternative. The use of the full multiphase Eulerian approach in

which each droplet size is considered to form a separate disperse phase is rather computationally intensive and reduces the gained benefits over the Lagrangian approach. To circumvent this problem and reduce the number of coupled equations to be solved, researchers have followed two routes within the Eulerian framework. The first track is denoted by the methods of moments [9-14] in which the disperse phase is considered to represent a set of continuous media with the spray described by a set of conservation equations obtained by taking the moments of the velocity variable at each droplet size and space location. At high accuracy, the cost of the method is lower but comparable to the Lagrangian approach [12]. The second alternative method, pursued here, follows the population balance approach [15], in which a population balance equation for each disperse phase, representing the transport of the number density of the phase through space, is used to trail the size distribution of the particles. As reported in [12] the extension of the method to sprays has not yet received a satisfactory answer.

In this work, the numerical foundations for the simulation of supersonic droplet mixing and evaporation are developed. This is achieved by following an Eulerian approach using: (i) the full multiphase flow model, (ii) the Multi-Size-Group model (MUSIG), and (iii) the Heterogeneous Multi-Size-Group model (H-MUSIG). To the authors' knowledge, MUSIG and H-MUSIG have been extensively used in solving for low speed bubbly flows but have not been used for predicting the evaporation of liquid droplets flowing in a high speed gas flow. It is the objective of this study to accomplish this task by extending these models to allow predicting mixing and evaporation of liquid droplets injected into a stream of gas flowing at any speed (i.e. from low subsonic to high supersonic speed). For that purpose, the above-mentioned three approaches are embodied within an all speed pressure-based finite volume flow solver in which a droplet evaporation model is implemented. The k-ε[16] two-equation turbulence model is used to account for the droplet-gas turbulence with

modifications for supersonic flows. Droplet turbulence is estimated using an algebraic model based on the Boussinesq approach [7,17,18]. Different droplet sizes are considered and droplet breakup and coalescence [19,20] are modeled and their effects incorporated into the conservation equations via source terms.

In the remainder of this article, the governing conservation equations for both gas and liquid droplet phases and their discretization procedures are first presented. This is followed by a detailed description of the three solution methodologies. The resulting algorithms are used to solve two physical configurations involving streamwise and cross-stream injection into a subsonic and supersonic stream flowing in a rectangular domain. Results presented in the form of droplet and gas velocity, pressure, gas temperature, vapor mass fraction, air volume fraction, gas density, and gas turbulent viscosity fields and profiles are compared and conclusions drawn.

#### THE GOVERNING EQUATIONS

Starting from the Navier-Stokes equations, instantaneous transport equations for the gas and droplet phases can be derived either by spatial, temporal, or ensemble averaging [21,22]. However, these transport equations can only be used for the description of sprays in laminar gas flows. In the turbulent regime, the system of equations is extended by introducing turbulent fluctuations of the transport quantities followed by Reynolds averaging of the equations. The interacting flow fields are described by the transport equations presented next.

## **GAS EQUATIONS**

The continuity, momentum, energy, turbulence kinetic energy, and turbulence dissipation rate equations for the gas phase, which is composed of two species namely air and vapor, in

addition to the mass fraction equation of the fuel vapor in the gaseous phase, are respectively written as

$$\frac{\partial}{\partial t} \left( \alpha_{g} \rho_{g} \right) + \nabla \cdot \left( \alpha_{g} \mathbf{u}_{g} \rho_{g} \right) = \nabla \cdot \left( \frac{\mu_{t,g}}{Sc_{t,g}} \nabla \alpha_{g} \right) + \dot{M}_{vap,g}$$

$$\tag{1}$$

$$\frac{\partial}{\partial t} (\alpha_g \rho_g \mathbf{u}_g) + \nabla \cdot (\alpha_g \rho_g \mathbf{u}_g \mathbf{u}_g) = -\alpha_g \nabla p + \nabla \cdot \overline{\tau}_g + \mathbf{F}_g^B + \mathbf{F}_g^D + \dot{M}_{vap,g} \mathbf{u}_d$$
 (2)

$$\frac{\partial}{\partial t} (\alpha_{g} \rho_{g} k_{g}) + \nabla \cdot (\alpha_{g} \rho_{g} \mathbf{u}_{g} k_{g}) = \nabla \cdot (\alpha_{g} \mu_{eff,k,g} \nabla k_{g}) + \alpha_{g} (P_{k} - \rho_{g} \varepsilon_{g}) + S_{k,d}$$
(3)

$$\frac{\partial}{\partial t} \left( \alpha_{g} \rho_{g} \varepsilon_{g} \right) + \nabla \cdot \left( \alpha_{g} \rho_{g} \mathbf{u}_{g} \varepsilon_{g} \right) = \nabla \cdot \left( \alpha_{g} \mu_{eff, \varepsilon, g} \nabla \varepsilon_{g} \right) + \alpha_{g} \left( C_{\varepsilon 1} \frac{\varepsilon_{g}}{k_{g}} P_{k} - C_{\varepsilon 2} \rho_{g} \frac{\varepsilon_{g}^{2}}{k_{g}} \right) + S_{\varepsilon, d}$$
(4)

$$\frac{\partial}{\partial t} \left( \alpha_{g} \rho_{g} h_{g} \right) + \nabla \cdot \left( \alpha_{g} \rho_{g} \mathbf{u}_{g} h_{g} \right) = \nabla \cdot \left( \dot{q}_{g} \right) + \nabla \cdot \left( \frac{\mu_{t,g}}{\Pr_{t}} \nabla h_{g} \right) + S_{h,g} + \dot{M}_{vap,g} h_{vap,g}$$
(5)

$$\frac{\partial}{\partial t} \left( \alpha_{g} \rho_{g} Y_{vap,g} \right) + \nabla \cdot \left( \alpha_{g} \rho_{g} \mathbf{u}_{g} Y_{vap,g} \right) = \nabla \cdot \left( \alpha_{g} \Gamma_{Y_{vap,g,eff}} \nabla Y_{vap,g} \right) + \dot{M}_{vap,g} \left( \mathbf{I} - Y_{vap,g} \right)$$

$$(6)$$

In equation (2), the inter-phase coupling force  $\mathbf{F}_g^D$  is evaluated as described in Appendix I.

## **DROPLET BALANCE EQUATIONS**

Several models of varying degrees of complexity have been developed for simulating droplet evaporation. The first model which was developed almost half a century ago is the D<sup>2</sup> model of Godsave and Spalding [23, 24]. The derivation of this model is based on the assumptions of constant thermo-physical properties, constant gas temperature, and constant droplet temperature with its value set equal to the liquid boiling temperature. An improvement to this model referred to as either the infinite conductivity model or the uniform temperature model was developed [25-27]. In the improved model, it is assumed that the characteristic timescales for energy distribution inside the droplet are much smaller than the droplet lifetime [28], thus the temperature distribution inside the droplet is uniform but varies with time and location. Another approach to simulate droplet evaporation is provided by the Thin Skin (TS) model [28]. In the TS model the droplet lifetime is assumed to be very small as compared to the characteristic time scales for the liquid phase transport processes. With this

approximation, internal droplet heating becomes negligible and the droplet temperature remains constant at its initial value. However, the fundamental element in the model is the introduction of a virtual layer of very small thickness at the droplet surface that controls the energy transfer from the surrounding gas to the droplet. A more sophisticated approach is provided by the Conduction Limit model which attempts to overcome the assumption of a uniform droplet temperature by assuming temperature gradients in the radial direction inside the droplet [28]. This consideration requires solving an energy equation in the radial direction of the droplet interior in order to calculate the droplet internal temperature, which is an expensive task. An easier method taking into consideration variation in temperature within the droplet is provided by the Temperature Profile models [29, 30]. In these models, instead of solving for the temperature variation within the droplet, a droplet temperature profile is assumed. With this assumption, the heat balance equation at the droplet surface can be satisfied, but not inside the droplet. The Temperature Profile models have improved predictions of fuel heating and evaporation in diesel engines [28]. Another model accounting for internal circulation within the droplet is denoted by the Effective Conductivity model [31, 32]. In this model, an effective conductivity for the droplets in terms of the liquid Peclet number, taking into consideration internal circulation, is used. Another improvement to the classical D<sup>2</sup> model is provided by the evaporation model developed by Abramzon and Sirignano [33,34], which accounts for the effects of variable thermo-physical properties, nonunitary gaseous Lewis number, and the Stefan flow on heat and mass transfer between the droplet and the gas as well as internal circulation and transient heating.

Recently, Miller et al. [35] reported on a study evaluating the performance of several evaporation models. Their findings indicated that all investigated models performed nearly identically for low evaporation rates. At high evaporation rates, large deviations were found between the various model predictions. Because the intention of this paper is to extend the

applicability of MUSIG and H-MUSIG to predict mixing and evaporation of liquid droplets injected into a stream of gas flowing at any speed and since the rate of evaporation involved is low, as a compromise between accuracy and computational cost, droplet evaporation is simulated by means of the Uniform Temperature model [36, 37]. The analytical derivation of this model does not consider contributions to heat and mass transport through forced convection by the gas flow around the droplet. Forced convection is taken into account by means of two empirical correction factors  $(m_{correction} \text{ and } h_{correction})$  [38]. The conservation equations for the droplet phases are given as

$$\frac{\partial}{\partial t} \left( \alpha_{d,i} \rho_{d,i} \right) + \nabla \cdot \left( \alpha_{d,i} \mathbf{u}_{d,i} \rho_{d,i} \right) = \nabla \cdot \left( \frac{\mu_{t,d,i}}{Sc_{t,d,i}} \nabla \alpha_{d,i} \right) + \dot{M}_{d,i}$$
(7)

$$\frac{\partial}{\partial t} \left( \alpha_{d,i} \rho_{d,i} \mathbf{u}_{d,i} \right) + \nabla \cdot \left( \alpha_{d,i} \rho_{d,i} \mathbf{u}_{d,i} \mathbf{u}_{d,i} \right) = -\alpha_{d,i} \nabla p + \mathbf{F}_{d,i}^{B} + \mathbf{F}_{d,i}^{D} + \dot{M}_{d,i} \mathbf{u}_{d,i}$$
(8)

$$\frac{\partial}{\partial t} \left( \alpha_{d,i} \rho_{d,i} h_{d,i} \right) + \nabla \cdot \left( \alpha_{d,i} \rho_{d,i} \mathbf{u}_{d,i} h_{d,i} \right) = \nabla \cdot \left( \alpha_{d,i} \frac{\mu_{t,d,i}}{\operatorname{Pr}_{t,d,i}} \nabla h_{d,i} \right) +$$

$$h_{d,i} \nabla \cdot \left( \frac{\mu_{t,d,i}}{\operatorname{Sc}_{t,d,i}} \nabla \alpha_{d,i} \right) + \pi d_{i}^{2} \beta^{*} \left( T_{g} - T_{d,i} \right) + \dot{M}_{d,i} \left( \Delta h_{v} + h_{d,i} \right)$$
(9)

where

$$\sum_{i} \dot{M}_{d,i} = -\dot{M}_{vap} = -\sum_{i} \frac{6\alpha_{d,i}}{\pi d_{i}^{3}} \dot{m}_{vap,i}^{*}$$
(10)

$$\dot{m}_{vap,i}^* = m_{correction,i} \dot{m}_{vap,i} \tag{11}$$

$$\dot{Q}_{cond,s,i}^* = \pi d_i^2 \alpha_i^* \left( T_{d,i} - T_g \right) \tag{12}$$

$$\dot{H}_{vap,s,i}^* = \dot{m}_{vap,i}^* c_{p,vap,ref,i} \left( T_{d,i} - T_g \right) \tag{13}$$

$$\dot{m}_{vap,i} = 2\pi d_i \rho_{g,ref,i} \Gamma_{im,ref,i} L n \frac{1 - Y_{vap,g,i}}{1 - Y_{vap,g,i}}$$

$$(14)$$

$$\beta_{i}^{*} = h_{correction,i} \frac{\frac{\dot{m}_{vap,i} c_{p,vap,ref,i}}{\pi d_{i}^{2}}}{\exp\left(\frac{\dot{m}_{vap,i} c_{p,vap,ref,i}}{2\pi d_{i} \lambda_{g,ref,i}}\right) - 1}$$

$$(15)$$

$$m_{correction,i} = 1 + 0.276 \,\text{Re}_{d,i}^{1/2} \,Sc_i^{1/3}$$
 (16)

$$h_{correction,i} = 1 + 0.276 \,\text{Re}_{d,i}^{1/2} \,\text{Pr}_{i}^{1/3} \tag{17}$$

$$\mu_{turb,d,i} = \mu_{turb,g} \frac{\rho_{d,i}}{\rho_g} \frac{k_{d,i}}{k_g}$$
 (18)

For an N-phase flow, the volume fractions  $\alpha^{(k)}$  are characterized by the following condition:

$$\sum_{k=1}^{N} \alpha^{(k)} = 1 \tag{19}$$

The ratio of the turbulent kinetic energies of a dispersed (d) and gas (g) phase is calculated using the approach in [7,18] as

$$\frac{k_d}{k_g} = \frac{1}{1 + \omega^2 \tau^2} \tag{20}$$

where

$$k_d = \frac{1}{2} \mathbf{u}_d' \cdot \mathbf{u}_d' \tag{21}$$

Since in general the droplets do not follow the motion of the surrounding fluid from one point to another it is expected for the ratio  $k_d / k_g$  to be different from unity and varies with particle relaxation time t and local turbulence quantities. Krämer [18] recommends the following equation for the frequency of the particle response:

$$\omega = \frac{1}{\tau} \left( \frac{\sqrt{\frac{2}{3} k_g}}{L_x} \tau \right)^{1/4}$$

$$\tau = \frac{1}{18} \frac{\rho_d}{\rho_g} \frac{D^2}{v} \frac{1}{1 + 0.133 \text{Re}_d^{0.687}}$$
(22)

with a characteristic macroscopic length scale of turbulence given by

$$L_{x} = \left(c_{\mu}\right)^{3/4} \frac{\left(k_{g}\right)^{3/2}}{\varepsilon_{g}} \tag{23}$$

## **DISCRETIZATION PROCEDURE**

A review of the above differential equations reveals that they are similar in structure. If a typical representative variable associated with phase (k) is denoted by  $\phi^{(k)}$ , the general fluidic differential equation may be written as

$$\frac{\partial \left(\alpha^{(k)} \rho^{(k)} \phi^{(k)}\right)}{\partial t} + \nabla \cdot \left(\alpha^{(k)} \rho^{(k)} \mathbf{u}^{(k)} \phi^{(k)}\right) = \nabla \cdot \left(\alpha^{(k)} \Gamma^{(k)} \nabla \phi^{(k)}\right) + \alpha^{(k)} Q^{(k)}$$
(24)

where the expression for  $\Gamma^{(k)}$  and  $Q^{(k)}$  can be deduced from the parent equations.

The general conservation equation (24) is integrated over a finite volume to yield

$$\iint_{\Omega} \frac{\partial \left(\alpha^{(k)} \rho^{(k)} \phi^{(k)}\right)}{\partial t} d\Omega + \iint_{\Omega} \nabla \cdot \left(\alpha^{(k)} \rho^{(k)} \mathbf{u}^{(k)} \phi^{(k)}\right) d\Omega = \iint_{\Omega} \nabla \cdot \left(\alpha^{(k)} \Gamma^{(k)} \nabla \phi^{(k)}\right) d\Omega + \iint_{\Omega} \alpha^{(k)} Q^{(k)} d\Omega \tag{25}$$

where  $\Omega$  is the volume of the control cell. Using the divergence theorem to transform the volume integral into a surface integral, replacing the surface integrals by a summation of the fluxes over the sides of the control volume, and then discretizing these fluxes using suitable interpolation profiles the following algebraic equation results:

$$A_P^{(k)}\phi_P^{(k)} = \sum_{NB} A_{NB}^{(k)}\phi_{NB}^{(k)} + B_P^{(k)}$$
(26)

In compact form, the above equation can be written as

$$\phi^{(k)} = H_P \left[ \phi^{(k)} \right] = \frac{\sum_{NB} A_{NB}^{(k)} \phi_{NB}^{(k)} + B_P^{(k)}}{A_P^{(k)}} \tag{27}$$

An equation similar to equation (26) or (27) is obtained at each grid point in the domain and the collection of these equations forms a system that is solved iteratively.

The discretization procedure for the momentum equation yields an algebraic equation of the form

$$\mathbf{u}_{P}^{(k)} = \mathbf{H} \mathbf{P}_{P} \left[ \mathbf{u}^{(k)} \right] - \alpha^{(k)} \mathbf{D}_{P}^{(k)} \nabla_{P} \left( P \right)$$
(28)

Furthermore, the phasic mass-conservation equation can be viewed as a phasic volume fraction equation, which can be written as

$$\alpha_P^{(k)} = H_P \left\lceil \alpha^{(k)} \right\rceil \tag{29}$$

or as a phasic continuity equation to be used in deriving the pressure correction equation, in which case it is rearranged into

$$\frac{\left(\alpha_{P}^{(k)}\rho_{P}^{(k)}\right) - \left(\alpha_{P}^{(k)}\rho_{P}^{(k)}\right)^{Old}}{\delta t}\Omega + \sum_{f}\alpha_{f}^{(k)}\rho_{f}^{(k)}\mathbf{u}_{f}^{(k)} \cdot \mathbf{S}_{f} = \alpha_{P}^{(k)}\dot{M}_{P}^{(k)}$$

$$(30)$$

## PRESSURE CORRECTION EQUATION

To derive the pressure-correction equation, the mass conservation equations of the various fluids are added to yield the global mass conservation equation given by

$$\sum_{k} \left\{ \frac{\left(\alpha_{P}^{(k)} \rho_{P}^{(k)}\right) - \left(\alpha_{P}^{(k)} \rho_{P}^{(k)}\right)^{Old}}{\delta t} \Omega + \sum_{f} \alpha_{f}^{(k)} \rho_{f}^{(k)} \mathbf{u}_{f}^{(k)} . \mathbf{S}_{f} \right\} = 0$$

$$(31)$$

Denoting the corrections for pressure, velocity, and density by  $\mathbf{P}'$ ,  $\mathbf{u}^{(k)'}$ , and  $\rho^{(k)'}$ , respectively, the corrected fields are written as

$$P = P^{\circ} + P', \mathbf{u}^{(k)} = \mathbf{u}^{(k)^*} + \mathbf{u}^{(k)'}, \rho^{(k)} = \rho^{(k)\circ} + \rho^{(k)'}$$
(32)

Combining equations (28), (31), and (32), the final form of the pressure-correction equation is obtained as [39]

$$\sum_{k} \left\{ \frac{\Omega}{\delta t} r_{p}^{(k)o} C_{\rho}^{(k)} P_{p}' + \sum_{f} r_{f}^{(k)o} U_{f}^{(k)*} C_{\rho}^{(k)} P_{f}' - \sum_{f} r_{f}^{(k)o} \rho_{f}^{(k)*} \left( r_{f}^{(k)o} \mathbf{D}_{f}^{(k)} \nabla P_{f}' \right) \mathbf{S}_{f} \right\} \\
= -\sum_{k} \left\{ \frac{r_{p}^{(k)o} \rho_{p}^{(k)*} - \left( r_{p}^{(k)o} \rho_{p}^{(k)*} \right)^{old}}{\delta t} \Omega + \sum_{f} r_{f}^{(k)o} \rho_{f}^{(k)*} U_{f}^{(k)*} \right\}$$
(33)

The corrections are then applied to the velocity, density, and pressure fields using the following equations:

$$\mathbf{u}_{P}^{(k)*} = \mathbf{u}_{P}^{(k)\circ} - r^{(k)\circ} \mathbf{D}_{P}^{(k)} \nabla_{P} P', \quad P^{*} = P^{\circ} + P', \quad \rho^{(k)*} = \rho^{(k)\circ} + C_{\rho}^{(k)} P'$$
(34)

## THE MULTIPHASE FLOW MODEL

In the multiphase model, displayed schematically in Figure 1, the dispersed phase is subdivided into N size groups where each group is treated as a phase in the calculation.

Because of that the number of coupled equations associated with this model is very large, which limits in practice the number of size groups that can be used due to the extensive numerical effort required to solve the involved coupled equations.

In order to keep track of the droplet size, an additional diameter equation is solved for every droplet phase. This equation is derived based on mass conservation and is given by

$$\frac{\partial}{\partial t} \left( \alpha_{d,i} \rho_{d,i} d_i \right) + \nabla \cdot \left( \alpha_{d,i} \rho_{d,i} \mathbf{u}_{d,i} d_i \right) = \nabla \cdot \left( \alpha_{d,i} \frac{\mu_{t,d,i}}{\sigma_{t,d,i}} \nabla d_i \right) + d_i \nabla \cdot \left( \frac{\mu_{t,d,i}}{Sc_{t,d,i}} \nabla \alpha_{d,i} \right) + \frac{4}{3} d_i \dot{M}_{d,i} \tag{35}$$

The evaporation source term appearing in the continuity, momentum, energy, and droplet diameter equations is inversely proportional to the square of the droplet diameter. As the droplet diameter decreases due to evaporation, the time-scale associated with evaporation decreases and becomes smaller than the flow-solver time-scale. To overcome convergence difficulty associated with this time-scale disparity, many numerical enhancement techniques are implemented within the multiphase flow solver. The coupling between the momentum equations of the various phases is improved through the use of the SImultaneous solution of Non-linearly Coupled Equations (SINCE) [40] technique, which is and extension into Nphase flow of the Partial Elimination Algorithm [41] applicable to two-phase flow. Moreover, in order for the pressure correction to drive all phases to conservation equally (gas and liquid), a weighted pressure correction equation is constructed by normalizing the individual continuity equations via a weighting factor (e.g. a reference density) [43], in such a way that their coefficients become of comparable magnitude. Further, the solution of the volume fraction equations is improved by implicitly accounting for the influence of the volume fractions of the different phases on each other and then bounding the resulting fields as detailed in [39]. Furthermore, under-relaxation of the equations is done following a false transient approach allowing different false time steps to be used for the various equations and in the different phases. In addition to the above, as droplets evaporate their sizes tend to zero causing the evaporation source terms to become singular and creating numerical difficulties.

To circumvent this hurdle, a condition is imposed whereby a droplet is spontaneously evaporated whenever its diameter becomes smaller than a threshold value (a value of 1  $\mu$ m was used in this work). Once the diameter is set to zero, the corresponding source terms are also set to zero eliminating the singularity.

This multi-phase model is an extension of the work performed in [43]. Results generated using this model are the baseline against which results generated using the MUSIG and H-MUSIG models are compared.

## FULL MULTIPHASE SOLUTION PROCEDURE

The overall solution procedure is an extension of the single-phase SIMPLE algorithm [44,45] into multi-phase flows [39]. The sequence of events in the multiphase algorithm is as follows:

- 1. Solve the fluidic momentum equations for velocities.
- 2. Solve the pressure correction equation based on global mass conservation.
- 3. Correct velocities, densities, and pressure.
- 4. Solve the fluidic mass conservation equations for volume fractions.
- 5. Solve the fluidic scalar equations  $(k, \varepsilon, T, Y, D, \text{ etc...})$ .
- 6. Return to the first step and repeat until convergence.

# THE MULTI-SIZE-GROUP MODEL (MUSIG)

The MUSIG (MUltiple-SIze-Group) model [46,47] was originally developed for the prediction of bubbles in water and has never been used for the prediction of mixing and evaporation of liquid droplets in a stream of gas. It is the intention of this work to extend the applicability of MUSIG to such configuration.

As a first step for describing the MUSIG model, an explanation of the population balance approach is provided. This is followed by the model description, the equations involved, and the break up and coalescence models used.

## POPULATION BALANCE APPROACH

In spray modeling, a wide range of particle sizes and shapes exist at every point in the dispersed phase, which makes the description of the size and shape of the droplets very difficult. This difficulty is further magnified when break up and coalescence occur due to their great influence on the flow fields. Therefore it is essential in modeling spray flows to use a formulation that takes into account the different size distribution of particles in addition to the birth and death processes that may be encountered [48]. This is accomplished through the use of the population balance approach.

Population balance [15] represents the transport of the number density of the fluid through space taking into account birth and death of particles due to breakup and coalescence. The number density transport equation of particles having volume  $v_i$ , i.e. group size i, is given by

$$\frac{\partial n_i}{\partial t} + \nabla . (\mathbf{u} n_i) = S_i + (S_{ph})_i \tag{36}$$

The interaction term  $S_i$  represents the net rate of change in the number density distribution function,  $n_i$ , due to particle break-up and coalescence. A general representation of these source and sink terms is given as

$$S_i = B_{Bi} - D_{Bi} + B_{Ci} - D_{Ci} (37)$$

Moreover the term  $S_{ph}$  is added to the population balance equation (Eq. (36)) in order to account for phase change since size change can occur because of birth due to nucleation, condensation and evaporation [49,50].

#### MUSIG MODEL DESCRIPTION

In this model, displayed schematically in Figure 2, the dispersed phase is decomposed into N size groups, which are assumed to be moving at the same speed. However, the size distribution is taken into consideration by solving N continuity or population balance equations. The single disperse phase is thus characterized by various size groups, from which a local Sauter diameter is computed. An accurate determination of the droplet Sauter diameter is crucial in order to calculate the interfacial area based on which the interphase heat and mass transfer and momentum drags could be evaluated.

## MUSIG MODEL FORMULATION

As described previously a continuity equation for each size group (a population balance equation) is solved, but it is assumed that all droplets move with the same velocity so that only one set of momentum equations for the dispersed phase has to be solved.

If  $f_i$  denotes the size fraction of the polydispersed phase which appears in size group i (i.e.  $f_i = \alpha_i / \alpha_d$ ) and  $\rho_d$  denotes the density of the dispersed phase, then Equation (36) can be rewritten as

$$\frac{\partial}{\partial t} \left( \rho_d \alpha_d f_i \right) + \nabla \cdot \left( \rho_d \alpha_d f_i \mathbf{u}_i \right) = S_i + \left( S_{ph} \right)_i \tag{38}$$

Since this model assumes that all particles have the same velocity,  $\mathbf{u}_i$  is replaced by  $\mathbf{u}_d$  (velocity of the dispersed phase) and the population fraction equation is reduced to

$$\frac{\partial}{\partial t} \left( \rho_d \alpha_d f_i \right) + \nabla \cdot \left( \rho_d \alpha_d f_i \mathbf{u}_d \right) = S_i + \left( S_{ph} \right)_i \tag{39}$$

This equation has the form of the transport equation of a scalar variable  $f_i$  in which the source term  $S_i$  accounts for: (i) the birth of droplets of size i due to breakup of droplets of larger size and coalescence of droplets of smaller size; and (ii) the death of droplets of size i due to both

break up and coalescence encountered in this size group. Therefore the sum of this term over all size groups is equal to zero

$$(40)$$

If summation over all size groups is performed, an overall continuity equation for the dispersed phase is derived. Performing this summation and noticing that  $\sum_{i=1,N} f_i = 1$ , the overall continuity equation for the dispersed phase is found as

$$\frac{\partial}{\partial t} (\alpha_{d} \rho_{d} f_{1}) + \nabla \cdot (\alpha_{d} \mathbf{u}_{d} \rho_{d} f_{1}) = S_{1} - f_{1} \dot{M}_{vap,g}$$

$$\frac{\partial}{\partial t} (\alpha_{d} \rho_{d} f_{2}) + \nabla \cdot (\alpha_{d} \mathbf{u}_{d} \rho_{d} f_{2}) = S_{2} - f_{2} \dot{M}_{vap,g}$$

$$\vdots \vdots$$

$$\frac{\partial}{\partial t} (\alpha_{d} \rho_{d} f_{N}) + \nabla \cdot (\alpha_{d} \mathbf{u}_{d} \rho_{d} f_{N}) = S_{N} - f_{N} \dot{M}_{vap,g}$$

$$\frac{\partial}{\partial t} (\alpha_{d} \rho_{d} f_{N}) + \nabla \cdot (\alpha_{d} \mathbf{u}_{d} \rho_{d} f_{N}) = -\dot{M}_{vap,g}$$

$$\frac{\partial}{\partial t} (\alpha_{d} \rho_{d}) + \nabla \cdot (\alpha_{d} \mathbf{u}_{d} \rho_{d}) = -\dot{M}_{vap,g}$$
(41)

After solving the population balance equations, the droplet Sauter diameter, which represents an average depiction of the dispersed phase, is calculated as

$$\frac{1}{d_S} = \sum_{i=1}^{N} \left( \frac{f_i}{d_i} \right) \tag{42}$$

where  $d_i$  is the diameter of size group i.

The MUSIG model essentially reduces the multiphase approach described above back to a two-fluid approach with one velocity field for the continuous phase and one for the dispersed phase. However, the continuity equations of the particle size groups are retained and solved to represent the size distribution. With this approach, it is possible to consider a larger number of particle size groups (say 10, 20 or even 30 particle phases) to give a better representation of the size distribution.

As mentioned earlier, the MUSIG model (and H-MUSIG, to be presented later) was developed for the study of bubbles in liquids and has not been used to predict evaporation of liquid droplets in gases. When used for that purpose, several issues arise and have to be addressed. The main assumption in MUSIG is classes of pre-assigned sizes. Since evaporation causes droplets to decrease in size, it should be reflected in the evaporation rate. This is done by replacing the droplet diameter in Equation (14) by the Sauter diameter for calculating the evaporated mass flux. The decrease in the droplet sizes is expected to be reflected by the Sauter diameter through the shift in the population fractions to lower diameters. The overall decrease in the droplet mass due to evaporation is obtained from the decrease in the droplet volume fraction (e.g. Equation 7). Since one evaporation mass flux is calculated, an assumption needs to be made with regard to its subdivision among the various size groups needed in solving the population fraction equations. In this work, a size group portion is calculated by multiplying the total mass flux by the respective population fraction, which allows overall mass conservation to be satisfied (Equation 41).

## **BREAK UP AND COALESCENCE MODELS**

The models that have been used for the break-up and coalescence rates are due to Luo and Svendsen [19] and Coulaloglou and Tavlarides [20], respectively. A summary of these models is given next.

## LUO AND SVENDSEN BREAKUP MODEL

The net source to group i due to breakup is witten as

$$B_{Bi} - D_{Bi} = \rho_d \alpha_d \left( \sum_{j>i} B_{ji} f_j - f_i \sum_{j

$$\tag{43}$$$$

The break-up rate  $B_{ij}$  is assumed to be a function of the break-up fraction  $B'_{ij}$  as follows:

$$B_{ij} = B'_{ij} \int_{f_{BV}} df_{BV} \tag{44}$$

The breakage volume fraction is assumed to be given by

$$f_{BV} = \frac{m_i}{m_j} = \frac{d_i^3}{d_j^3} \tag{45}$$

where  $d_j$  is the diameter of a mother particle splitting into two particles of sizes  $d_i$  and  $\left(d_j^3 - d_i^3\right)^{1/3}$ . The break-up frequency of a mother particle with size  $d_j$  splitting into two particles of sizes  $d_i$  and  $\left(d_j^3 - d_i^3\right)^{1/3}$  is obtained as

$$B'_{ji} = 0.923 F_B (1 - \alpha_d) \left( \frac{\varepsilon_c}{d_j^2} \right)^{1/3} \underbrace{\int_{\xi_{min}} \frac{(1 + \xi)^2}{\xi^{11/3}} e^{-\frac{12\sigma \left( \frac{2J^3}{BV} + (1 - f_{BV})^{2J^3} - 1 \right)}{\beta \rho_c \varepsilon_c^{2J^3} d_j^{5/3} \xi^{11/3}} d\xi}_{I}$$

$$(46)$$

where  $F_B$  is added as a calibration factor of the model,  $\varepsilon_c$  is the continuous phase eddy dissipation energy,  $\sigma$  is the surface tension,  $\beta$ =2, and  $\xi$  is the dimensionless size of eddies in the inertial subrange of isotropic turbulence. The lower limit of the integration is given by

$$\xi_{\min} = 11.4 \frac{\eta}{d_i} \tag{47}$$

and the Kolmogorov micro-scale η is given by:

$$\eta = \left[ \left( \mu_c / \rho_c \right)^3 / \varepsilon_c \right]^{1/4} \tag{48}$$

#### COULALOGLOU AND TAVLARIDES COALESCENCE MODEL

Collisions may happen due to various mechanisms however this model only considers the collisions of droplets due to turbulence, buoyancy and laminar shear.

The net source to group *i* due to coalescence, is given as

$$B_{Ci} - D_{Ci} = \left(\rho_d \alpha_d\right)^2 \left(\frac{1}{2} \sum_{j \le i} \sum_{k \le i} C_{jk} f_j f_k \frac{m_j + m_k}{m_j m_k} X_{jki} - \sum_j C_{ij} f_i f_j \frac{1}{m_j}\right)$$
(49)

where  $C_{ij}$  is the specific coalescence rate between groups i and j and  $X_{jki}$  represents the fraction of mass due to coalescence between groups j and k which goes into i and is written as

$$X_{jki} = \begin{cases} \frac{\left(m_{j} + m_{k}\right) - m_{i-1}}{m_{i} - m_{i-1}} & \text{if } m_{i-1} < \left(m_{j} + m_{k}\right) < m_{i} \\ \frac{m_{i+1} - \left(m_{j} + m_{k}\right)}{m_{i+1} - m_{i}} & \text{if } m_{i} < \left(m_{j} + m_{k}\right) < m_{i+1} \\ 1 & \text{if } m_{j} + m_{k} \ge m_{\max} = m_{i} \\ 0 & \text{otherwise} \end{cases}$$
(50)

$$\sum_{i} X_{jki} = 1 \quad \text{for all } j, k$$
 (51)

When summed over all size groups, the net source due to coalescence is zero.

The coalescence rate  $C_{ij}$  of the dispersed phase in a turbulent flow field is described as the product of the collision frequency  $\omega_c(d_i,d_j)$  and the corresponding coalescence efficiency  $\lambda_c(d_i,d_j)$  and is written as

$$C_{ii} = \omega_c \left( d_i, d_i \right) \lambda_c \left( d_i, d_i \right) \tag{52}$$

In the Coulaloglou and Tavlarides [20] model it is assumed that the mechanism of collision in a locally isotropic flow field is analogous to collisions between molecules as in kinetic theory of gases, the collision frequency between two drops with volumes  $\Omega_i$  and  $\Omega_j$  are expressed as

$$\omega_c \left( d_i, d_j \right) = K_c \frac{\varepsilon_c^{1/3}}{1 + \alpha_d} \left( d_i + d_j \right)^2 \left( d_i^{2/3} + d_j^{2/3} \right)^{1/2}$$
(53)

The coalescence efficiency is based on the film drainage mechanism where the drops are considered to cohere together and be prevented by coalescence by a film of continuous phase trapped between them. The coalescence efficiency as suggested by Coulaloglou and Tavlarides is given as

$$\lambda \left( \mathbf{d}_{i}, d_{j} \right) = \exp \left[ -K \frac{\mu_{c} \rho_{c} \varepsilon_{c}}{\sigma^{2} \left( 1 + \alpha_{d} \right)^{3}} \left( \frac{d_{i} d_{j}}{d_{i} + d_{j}} \right)^{4} \right]$$
(54)

#### MUISG SOLUTION PROCEDURE

The overall two-phase MUSIG solution procedure is as follows:

- 1. Solve the fluidic momentum equations for the gas and droplet velocities.
- 2. Solve the pressure correction equation based on global mass conservation.
- 3. Correct velocities, densities, and pressure.
- 4. Solve the fluidic mass conservation equations for droplet and air volume fractions.
- 5. Calculate sources due breakup and coalescence.
- 6. Solve the population fraction equations.
- 7. Calculate Sauter diameter.
- 8. Solve the fluidic scalar equations  $(k, \varepsilon, T, Y)$ .
- 9. Return to the first step and repeat until convergence.

# THE HETEROGENEOUS MUSIG MODEL (H-MUSIG)

With the MUSIG model, it is possible to consider a larger number of particle size groups to give a better representation of the size distribution. The shortcoming of this approach however [51, 52], is related to the droplet groups common velocity. It is well known that larger droplets do not follow the flow and smaller droplets do. By considering one average velocity for the droplets, a stratification of droplet sizes from normal fuel injection occurs

with larger droplets penetrating further into the flow. The larger droplets transport more fuel mass than may be expected. To alleviate this problem, it is proposed to extend the (homogeneous) MUSIG model into a Multi-phase MUSIG model or a Heterogeneous MUSIG model (H-MUSIG). In the extended model, rather than assigning one velocity for all droplet groups, classes of groups will be considered with droplet groups in a class sharing the same velocity. This suggested approach, displayed schematically in Figure 3, could be seen as a blend between a full multi-phase approach and a two-phase approach. If a group is composed of one droplet class, then the full multi-phase approach is obtained, whereas if a group is composed of all droplet sizes, then the original MUSIG is recovered.

## H-MUSIG MODEL DESCRIPTION AND FORMULATION

In this model, the dispersed phase is divided into N fields, each allowing an arbitrary number of sub-size classes [51,52]. Therefore N velocity fields are to be solved where each field is subdivided into  $M_l$  size groups moving at the same mean algebraic velocity.  $M_l$  population fraction equations need to be solved along with one set of momentum equations for each field.

If l denotes a group field number  $(l \in [1,N])$ , then the volume fractions of sub-classes, groups, and the dispersed phase are related through

$$\alpha_i = \alpha_d f_i = \alpha_{F_i} f_{F_i,i} \tag{55}$$

where  $f_i$  is the size fraction of the polydispersed phase which appears in group sub-size i,  $f_{F_l,i}$  is the population fraction of sub-group size i in the field l,  $\rho_d$  the density of the dispersed phase,  $\alpha_i$  is the volume fraction of sub-group size i and  $\alpha_{F_l}$  is the volume fraction of field l. The population fraction equation (Equation (36)) for each sub-size group in class field l can be written as

$$\frac{\partial}{\partial t} \left( \rho_d \alpha_{F_i} f_{F_i,i} \right) + \nabla \cdot \left( \rho_d \alpha_{F_i} f_{F_i,i} \mathbf{u}_{F_i} \right) = S_{F_i,i} + \frac{\alpha_{F_i}}{\alpha_d} f_{F_i,i} S_{ph}$$
(56)

Summing over all sub-classes in field *l* and applying the following additional relations

$$S_{F_{l}} = \sum_{i=1}^{M_{F_{k}}} S_{F_{l},i} \qquad \sum_{i=1}^{M_{F_{l}}} \frac{\alpha_{F_{l}}}{\alpha_{d}} f_{F_{l},i} = \frac{\alpha_{F_{l}}}{\alpha_{d}}$$
(57)

The continuity equation for each field or the volume fraction equation is found as

$$\frac{\partial}{\partial t} \left( \rho_d \alpha_{F_l} \right) + \nabla \cdot \left( \rho_d \alpha_{F_l} \mathbf{u}_{F_l} \right) = S_{F_l} + \frac{\alpha_{F_l}}{\alpha_d} S_{ph}$$
(58)

Additional relations and constraints are further added to this model as

$$\alpha_d = \sum_{l=1}^{N} \alpha_{F_l} = \sum_{i=1}^{N \times M} \alpha_i \qquad \sum_{i=1}^{M_{F_l}} f_{F_l,i} = 1 \qquad \sum_{i=1}^{N \times M} f_i = 1$$
 (59)

The source  $S_{F_{l,i}}$  is the net rate at which mass accumulates in sub-size group i due to coalescence of particles of smaller size than i in all field and breakup of particles of larger sizes than i in all fields. Mathematically  $S_{F_{l,i}}$  is given by

$$S_{F_l,i} = B_{i,B} - D_{i,B} + B_{i,C} - D_{i,C}$$
(60)

Here the birth and death rates are treated using specific breakup and coalescence models since they represent rates in the dispersed phase for all sub-classes with

$$S_{F_i} = \sum_{i=1}^{M_{F_i}} S_{F_i,i} \qquad \sum_{i=1}^{N} S_{F_i} = 0$$
 (61)

The overall continuity equation of the dispersed phase is derived by summing over all groups using the above mentioned relation and is found to be

$$\frac{\partial}{\partial t} (\rho_d \alpha_d) + \nabla \cdot (\rho_d \alpha_d \mathbf{u}_{F_l}) = S_{ph} \tag{62}$$

After solving the population balance equations for each sub-size group, the droplet Sauter diameter of the dispersed phase field *l* is calculated as

$$d_{s,F_l} = \frac{1}{\sum_{i=1}^{M_{F_l}} \frac{f_{F_l,i}}{d_i}}$$
(63)

For each field, the momentum equation that needs to be solved (since the velocities differ) is given by

$$\frac{\partial}{\partial t} \left( \rho_d \alpha_{F_l} \mathbf{u}_{F_l} \right) + \nabla \cdot \left( \rho_d \alpha_{F_l} \mathbf{u}_{F_l} \mathbf{u}_{F_l} \right) = -\alpha_{F_l} \nabla P + \\
\nabla \cdot \alpha_{F_l} \mu_{turb,d} \left( \nabla u_{F_l} + \nabla u_{F_l}^T \right) + \alpha_{F_l} \rho_d g + F_{F_l} + M_{F_l} + S_{M_{F_l}}$$
(64)

where  $M_{F_l}$  is the source term associated with momentum due to phase change,  $F_{F_l}$  is the momentum transfer between the dispersed phase l and the continuous phase, and  $S_{M_{F_l}}$  is the source term due to the transfer of momentum between different velocity groups due to breakup and coalescence processes leading to the formation of particles belonging to other groups.

## H-MUSIG MODEL SOLUTION STRATEGY

The solution algorithm of the H-MUSIG approach is as follows:

- 1. Solve the momentum equations for the dispersed and continuous phases.
- 2. Solve the Global continuity equation to calculate the pressure, which is shared by all phases.
- 3. Solve the continuity (volume fraction) equations to calculate the volume fractions of the dispersed phases (note that the volume fraction equations of the various phase fields include a source term due to particles breakup and coalescence).
- 4. Calculate sources due breakup and coalescence.
- 5. Solve the population fraction equations for the groups of each droplet phase.

- 7. Calculate Sauter diameters of the various phases.
- 8. Solve the fluidic scalar equations for all phases  $(k, \varepsilon, T, Y)$ .
- 9. Return to the first step and repeat until convergence.

## **NUMERICAL VALIDATION**

The above described solution algorithms are verified by numerically reproducing measurements in an isopropyl alcohol turbulent evaporating spray [53]. This problem has been used by several workers [54,55] to validate their numerical methods.

The experimental setup consists of a cylindrical test section of 194 mm inner diameter into which isopropyl alcohol with a temperature of 313 K is injected from a 20 mm outer diameter nozzle located along its axis of symmetry. The co-flowing air is simultaneously blown with a temperature of 373 K through a concentric annulus of 40 mm and 60 mm inner and outer diameter, respectively. The inlet mass flow rates of air and isopropyl alcohol are 28.3 g/s and 0.443 g/s, respectively. Detailed measurements at various axial positions are available for validating the numerical predictions. Radial profiles at x=3 mm are used to describe the inlet conditions to the domain, while profiles at x=25, 50, 100, and 200 mm are employed for comparison.

In the numerical solution obtained using the MUSIG model, the physical domain, considered to be axisymmetric of length 1m and radius 0.097m, is discretized using 130x80 non-uniform grids with denser clustering near the nozzle. The droplet phase is divided into 9 size groups with the diameter of the smallest droplet set to  $10\,\mu m$  and the increment to  $5\,\mu m$  (i.e. droplets of diameters between 10 and  $50\,\mu m$  are considered, the range suggested by experimental data [53] within which the bulk of the droplet sizes fall). The volume fraction and population fraction profiles of the various size groups at inlet are deduced from available experimental data.

Comparison of the numerically predicted radial profiles of the mean axial gas and droplet velocities against experimental data is presented in Figures 4(a) and 4(b), respectively. As shown numerical predictions at the four axial locations (x=25, 50, 100, and 200 mm) are in good agreement with experimental profiles. Comparison of the numerically predicted radial profiles of the turbulent gas and droplet kinetic energy against experimental data is presented in Figures 5(a) and 5(b), respectively. Unlike mean axial velocity profiles, fluctuating quantities are not as well predicted. This is not a defect in the numerical implementation of the solution algorithm but rather a characteristic of Reynolds-Averaged Navier-Stokes models, which predict well the mean fields but cannot capture well fluctuating quantities.

## **RESULTS AND DISCUSSION**

The capability of the various solution algorithms to predict turbulent evaporating sprays injected into streams flowing at all speeds is demonstrated in this section by presenting solutions to two two-dimensional problems. The physical situations for these problems are displayed in Figure 6. Figure 6(a) represents a rectangular duct in which air enters with a uniform free stream velocity U, while fuel (Kerosene is used in all subsequent computations) mixed with air is injected through a nozzle 2 mm in diameter in the streamwise direction through 120° angle. Figure 6(b) represents the same rectangular duct displayed in Figure 6(a) with fuel being injected in the cross-stream direction. The length of the domain is L and its width is W (W=L/4). Solutions for the above configurations are generated using the various methodology and results are compared.

## STREAMWISE INJECTION IN A RECTANGULAR DOMAIN

The physical domain depicted in Figure 6(a) is subdivided into 120x102 non-uniform control volumes (Figure 6(c)). The length L of the domain is 1 m. The fuel is injected through 12

uniform control volumes (each of width .001/12 m) at different injection angles (varying uniformly from -60° to 60° as shown in Figure 6(a)). In order to show the applicability of the solutions procedures for fluid flowing at all speeds, results for this configuration are generated for fuel injection in subsonic and supersonic streams. In both cases, the mixture of air and droplets are injected into the domain with a temperature of 350 K with the volume fraction of Kerosene in the injected air-fuel mixture being 0.1. The velocity of the injected mixture is set at 30 m/s. With this velocity profile and volume fraction a total of 1.8327 Kg/s/m of fuel are injected into the domain.

Full multiphase results are generated using 5 droplet phases of sizes 60 μm, 80 μm, 100 μm, 120 μm, and 140 μm with their inlet volume fractions being 0.0125, 0.0225, 0.03, 0.0225, and 0.0125 respectively. For the MUSIG model, the droplet phase is divided into 10 size groups with the diameter of the smallest droplet set to 55 μm and the increment to 10 μm with population fractions of 0.05, 0.075, 0.1, 0.125, 0.15, 0.15, 0.125, 0.1, 0.075, and 0.05, respectively. For the H-MUSIG model, two droplet phases are considered; each divided into five size groups discretized using the equal diameter discretization. The diameters and population fractions of the various groups are similar to those used with MUSIG.

## Evaporation and mixing of fuel droplets in a subsonic stream

For the physical situation depicted in Figure 6(a), the Mach number and temperature of the air at inlet to the domain are taken to be 0.2 ( $M_{air,inlet}$ =0.2) and 700 K, respectively. Comparison of results obtained using the various techniques are presented in Figures 7 through 10. Figure 7 displays the velocity fields for some of the droplet phases. Figures 7(a)-7(c) depict the velocity vectors for droplet phases 1 (60 µm in diameter), 3 (100 µm in diameter), and 5 (140 µm in diameter) using the full multiphase approach. H-MUSIG droplet velocity vectors are presented in Figures 7(d) and 7(e), while Figure 7(f) shows the droplet

vector field predicted using MUSIG. Both the multiphase and the H-MUSIG results reveal a larger droplet penetration with increasing droplet diameter, which is physically correct as larger particles possess higher inertia and are more capable of penetrating into the domain as compared to smaller ones, which align faster with the flow field. Further the path of the droplets predicted by MUSIG is between the trajectories of the smaller and larger droplet phases predicted by H-MUSIG (Compare Figure 7(f) against Figures 7(d) and 7(e)). The same is true for H-MUSIG and the full multiphase results (compare Figure 7(d) against Figures 7(a) and 76(b); and Figure 7(e) against Figures 7(b) and 7(c)).

Comparisons in the form of contour maps of the gas phase volume fraction, vapor mass fraction, gas density, and gas turbulent viscosity fields generated by the various methods are depicted in Figures 8(a)-8(d). As can be seen, the overall structure of the fields generated by the different methods is similar even though there are slight variations in the details. The volume fraction fields (Figure 8(a)) reflect the droplet velocity fields displayed in Figure 7, with the droplet volume fraction decreasing as droplets move in the domain. As expected, the vapor mass fraction (Figure 8(b)) in the gas phase maximizes at exit from the domain with the full multiphase results showing less evaporation in the region around the centerline of the domain. Density and turbulent viscosity field maps presented in Figure 8(c) and 8(d) show similar profiles with slight variation in values. This is further revealed by the profiles presented in Figure 9. In this figure, u-velocity, gas temperature, pressure, and vapor mass fraction profiles across the domain at x=0.5 generated using the various algorithms are compared. The gas u-velocity profiles (Figure 9(a)) obtained by the various methods are nearly coincident. The temperature profiles however (Figure 9(b)), show some differences in the region around the centerline of the domain, with H-MUSIG predicting the lowest gas temperature. This is in line with the vapor mass fraction contours presented earlier and the vapor mass fraction profiles in Figure 9(d), which reveal higher vapor mass fraction around the centerline, predicted by H-MUSIG and consequently lower gas temperature. Moreover, profiles in Figure 9(d) show that full multiphase results are close to H-MUSIG results in area away from the centerline and are close to MUSIG results in the region around the centerline. Pressure profiles presented in Figure 9(c) indicate slightly lower values ( $\approx$ 20 Pa) with the full multiphase approach. Values obtained by MUSIG and H-MUSIG are very close.

A comparison of the global behavior of the spray is presented in Figure 10. In this figure, the axial variation of the droplet average mass density (Figure 10(a)), turbulent kinetic energy (Figure 10(b)), temperature (Figure 10(c)), and relative axial velocity (Figure 10(d)) are displayed. These are calculated by the taking the area-averaged values at every axial station summed over all the droplet phases. Figure 10(a) indicates that the droplet mass density decreases in the streamwise direction due to evaporation. Moreover, the droplet velocity fluctuations increase close to the nozzle tip (Figure 10(b)) and decrease afterwards as the droplets become more aligned with the gas flow. Furthermore, Figure 10(c) shows that the rate of increase in the droplet temperature decreases in the flow direction due to the decrease in the gas temperature caused by the evaporating droplets. Finally, the acceleration of the droplets by the gas flow is reflected by the decrease in the difference between the droplet and gas axial velocity shown in Figure 10(d). As can be seen the three solutions exhibit similar behavior with profiles being close to each other. The plots also reveal that the largest differences are associated with the droplet turbulent kinetic energy (Figure 10(b)).

An important parameter for comparison is the percent of the injected fuel that has evaporated into the gas field. These percentages are found to be 30.83%, 27.78%, and 27.27% for the full multiphase method, the H-MUSIG model, and the MUSIG model respectively.

## Evaporation and mixing of fuel droplets in a supersonic stream

For the physical situation depicted in Figure 6(a), the Mach number and temperature of the air at inlet to the domain are taken to be 2 (M<sub>air,inlet</sub>=2) and 700 K, respectively. Comparison

of results obtained using the various techniques are presented in Figures 11 through 14. Figure 11 displays the velocity fields for some of the droplet phases. Figures 11(a)-11(c) depict the velocity vectors for droplet phases 1 (60 µm in diameter), 3 (100 µm in diameter), and 5 (140 µm in diameter) using the full multiphase approach. H-MUSIG droplet velocity vectors are presented in Figures 11(d) and 11(e), while Figure 11(f) shows the droplet vector field predicted using MUSIG. Due to the small velocity by which the fuel is injected (30 m/s) as compared to the gas velocity (1061 m/s) the spread is much lower than the subsonic case. Nevertheless, both the multiphase and the H-MUSIG results reveal a larger droplet penetration with increasing droplet diameter, which is physically correct as mentioned above. Further the path of the droplets predicted by MUSIG is between the trajectories of the smaller and larger droplet phases predicted by H-MUSIG (Compare Figure 11(f) against Figures 11(d) and 11(e)). The same is true for H-MUSIG and the full multiphase results (compare Figure 11(d) against Figures 11(a) and 11(b); and Figure 11(e) against Figures 11(b) and 11(c)).

Comparisons in the form of contour maps of the gas phase volume fraction, vapor mass fraction, gas density, and turbulent viscosity fields generated by the various methods are depicted in Figure 12. As in the previous case, the overall structure of the fields generated by the different techniques is similar, with differences being small. The volume fraction fields (Figure 12(a)) indicate a decrease as droplets move in the domain. As expected, the vapor mass fraction (Figure 12(b)) in the gas phase maximizes at exit from the domain with the full multiphase results showing higher evaporation in the region around the centerline of the domain. Density (Figure 12(c)) and turbulent viscosity (Figure 12(d)) contours generated by the various methods are similar with slight variation in values. This is further revealed in the comparison of profiles across the domain at x=0.5 presented in Figure 13. The gas u-velocity profiles (Figure 13(a)) are seen to be nearly coincident. The temperature profiles however

(Figure 13(b)), show a slight difference in the region around the centerline of the domain, with profiles predicted by MUSIG and H-MUSIG being almost coincident. Pressure profiles presented in Figure 13(c) show similar variations with values obtained with the full multiphase method being slightly higher. Moreover, profiles in Figure 13(d) show that H-MUSIG results are closer to the full multiphase results with the differences between the various profiles being in the region around the centerline.

As in the subsonic case, the streamwise variations in the droplet average mass density, turbulent kinetic energy, temperature, and relative axial velocity are computed and profiles generated by the various algorithms are displayed in Figures 14(a) through 14(d), respectively. As shown, solutions exhibit similar behavior with differences being slightly higher than in the subsonic case (Figure 10) with profiles generated by MUSIG and H-MUSIG in Figures 14(b) and 14(d) being closer to each other than those obtained using the full multiphase approach.

The percent of the injected fuel that has evaporated in the domain are calculated to be 11.15%, 12%, and 12.38% for the full multiphase method, the H-MUSIG model, and the MUSIG model respectively.

## CROSS-STREAM INJECTION IN A RECTANGULAR DOMAIN

The physical domain depicted in Fig. 6(b) is subdivided into 130x70 non-uniform control volumes. The length L of the domain is 1.1 m. The fuel is injected through 12 uniform control volumes (each of width .001/12 m) from two nozzles located on the lower and upper walls at 10 cm from the inlet. For both subsonic and supersonic cases, a total of 2.34 Kg/s/m of fuel are injected into the domain.

## Evaporation and mixing of fuel droplets in a subsonic stream

For the physical situation depicted in Figure 6(b), the Mach number and temperature of the air at inlet to the domain are taken to be 0.2 (M<sub>air,inlet</sub>=0.2) and 700 K, respectively. The Kerosene-air mixture is injected into the domain with a temperature of 350 K and a velocity of 30 m/s at an angle of 60° to the horizontal. The volume fraction of Kerosene in the mixture is 0.1. Full multiphase results are generated using 5 droplet phases of sizes 60 μm, 80 μm, 100 μm, 120 μm, and 140 μm with their inlet volume fractions being, respectively, 0.0125, 0.0225, 0.03, 0.0225, and 0.0125. For the MUSIG model, the droplet phase is divided into 10 size groups using the equal diameter discretization with the diameter of the smallest droplet set to 55 μm and the increment to 10 μm with population fractions of 0.05, 0.075, 0.1, 0.125, 0.15, 0.15, 0.125, 0.1, 0.075, and 0.05, respectively. For the H-MUSIG model, two variations are considered. In the first, two droplet phases are considered; each divided into five group sizes discretized using the equal diameter discretization. In the second, five droplet phases are considered, each divided into two group sizes using the equal diameter discretization. The diameters and population fractions of the various groups are similar to those used with MUSIG.

Comparison of results obtained using the various techniques are presented in Figures 15 through 19. Figures 15(a)-15(c) depict the velocity vectors for droplet phases 1 (60 µm in diameter), 3 (100 µm in diameter), and 5 (140 µm in diameter) using the full multiphase approach. H-MUSIG droplet velocity vectors, for the case with two droplet phases, are presented in Figures 15(d) and 15(e), while Figure 15(f) shows the droplet vector field predicted using MUSIG. As in the streamwise injection case, the multiphase and the H-MUSIG results reveal a relatively larger droplet penetration with increasing droplet diameter. Further the path of the droplets predicted by MUSIG is between the trajectories of the smaller and larger droplet phases predicted by H-MUSIG. The same is true for H-MUSIG and the

full multiphase results. Velocity vectors for the case when H-MUSIG is used with five droplet phases are presented in Figure 16. Similar behavior is observed with larger particles penetrating further into the domain.

Comparisons in the form of contour maps of the gas phase volume fraction, vapor mass fraction, gas density, and gas temperature fields generated by the various methods are depicted in Figure 17. With the injection velocity used, only the largest droplets are capable of penetrating into the central core of the domain close to the exit section. Contours generated by the various methods show similar overall behavior with slight differences in values, with the ones generated by H-MUSIG with five droplet phases being generally closer to contours obtained using the full multiphase method.

In Figure 18, the u-velocity, gas temperature, pressure, and vapor mass fraction profiles across the domain at x=0.6 (i.e. at 0.5 m from the nozzles) generated using the various algorithms are compared. As in the previous cases, the gas u-velocity (Figure 18(a)) component and gas temperature (Figure 18(b)) profiles are nearly coincident. Moreover, pressure values (Figure 18(c)) show a maximum difference of less than 50 Pa. Furthermore, vapor mass fraction profiles (Figure 18(d)) indicate that results generated by H-MUSIG with 5 droplet phases are on top of results obtained by the full multiphase approach in the wall region and deviate in the central portion of the domain. Nevertheless, the differences between values generated by the various methods are small.

The streamwise variations in the droplet average mass density, turbulent kinetic energy, temperature, and relative axial velocity are computed and profiles generated by the various algorithms are presented in Figure 19. As shown, profiles for the droplet mass density and droplet temperature are nearly coincident. This is not the case for the turbulent kinetic energy and the difference between the droplet and gas axial velocity profiles presented in Figures

19(b) and 19(d), which show slightly higher differences than those presented earlier. The trend of variation is, however, similar for all models.

The percentages of the injected fuel that has evaporated into the gas field as predicted by the various methods are found to be 29.89%, 27.38%, 27.35%, and 27.12% for the full multiphase method, the H-MUSIG model with five droplet phases, the H-MUSIG model with two droplet phases, and the MUSIG model respectively.

#### Evaporation and mixing of fuel droplets in a supersonic stream

The Mach number and temperature of the air at inlet to the domain shown in Figure 6(b) are taken to be 2 ( $M_{air,inlet}$ =2) and 700 K, respectively. The mixture of air and droplets are injected into the domain at a temperature of 350 K with the volume fraction of Kerosene in the injected air-fuel mixture set to 0.02. The velocity of the injected mixture is 75 m/s and the angle of injection is 60°.

Comparison of results obtained using the various techniques are presented in Figures 20 through 23. Figures 20(a)-20(c) depicts the velocity vectors for droplet phases 1 (60 µm in diameter), 3 (100 µm in diameter), and 5 (140 µm in diameter) using the full multiphase approach. H-MUSIG droplet velocity vectors are presented in Figures 20(d) and 20(e), while Figure 20(f) shows the droplet vector field predicted using MUSIG. Results exhibit the same behavior observed earlier with droplet trajectories predicted by MUSIG being between the trajectories of the smaller and larger droplet phases predicted by H-MUSIG. The same is true for H-MUSIG and the full multiphase results.

Comparisons in the form of contour maps of the gas phase volume fraction, vapor mass fraction, gas density, and gas turbulent viscosity fields generated by the various methods are depicted in Figure 21. The contours generated by the various methods are very close to each others indicating the validity of the various solution methodologies. This is further revealed by the u-velocity, gas temperature, pressure, and vapor mass fraction profiles across the

domain at x=0.6 (i.e. at 0.5 m from the nozzles) generated using the various algorithms depicted in Figure 22. As in the previous cases, the gas u-velocity (Figure 22(a)) component and gas temperature (Figure 22(b)) profiles are nearly coincident. Moreover, pressure values (Figure 22(c)) are closer then in the previous cases with MUSIG and H-MUSIG profiles being on top of each others. Furthermore, vapor mass fraction profiles displayed in Figure 22(d) indicate that H-MUSIG results are closer to the full multiphase results. Finally, the streamwise variation in the droplet fields generated using the various algorithms (Figures 23(a)-23(d)) reveal that results obtained by MUSIG and H-MUSIG are very close.

The percentages of the injected fuel that has evaporated into the gas field as predicted by the various methods are found to be 10.64%, 13.25%, and 13.41% for the full multiphase method, the H-MUSIG model, and the MUSIG model respectively.

### **CLOSING REMARKS**

Three numerical methods following a full multiphase approach, a MUlti-SIze Group (MUSIG) approach, and a Heterogeneous MUSIG (H-MUSIG) approach for the prediction of mixing and evaporation of liquid fuel injected into a stream of air flowing at any speed were developed. The numerical procedures were formulated, following an Eulerian approach, within a pressure-based fully conservative Finite Volume method. The k- $\epsilon$  two-equation model was used to account for the droplet and gas turbulence with modifications to account for compressibility at high speeds. The relative performance of the three approaches was assessed by solving for mixing and evaporation in two configurations involving droplets sprayed in the stream-wise and cross-stream directions in subsonic and supersonic streams. For the modeled cases, results indicated that solutions obtained by the various techniques exhibit similar behavior with differences in values being relatively small. Predictions generated using MUSIG and H-MUSIG could be improved through better representation of

evaporation in the population balance equations. Before being able to generalize the conclusions reported here, additional comparisons under different physical conditions are still required (e.g. high evaporation rates, highly turbulent separated and swirling flows, etc.).

This will form the subject of future developments.

## **ACKNOWLEDGMENTS**

This work has been support by The European Office for Aerospace Research and Development (EOARD) under grant number FA8655-06-1-3035.

### **APPENDIX** I

The inter-phase coupling force  $\mathbf{F}_g^D$  appearing in equation (2) is evaluated using

$$\mathbf{F}_{g}^{D} = -\sum_{i} \mathbf{F}_{d,i}^{D} = -\sum_{i} \frac{3}{4} \alpha_{d,i} \rho_{g} \frac{C_{D}}{d_{i}} \| \mathbf{u}_{g} - \mathbf{u}_{d,i} \| (\mathbf{u}_{g} - \mathbf{u}_{d,i}) = \sum_{i} A_{i}^{D} \mathbf{u}_{d,i} - \sum_{i} A_{i}^{D} \mathbf{u}_{g}$$
(A.1)

where  $C_{D,i}$  represents the drag coefficient of droplets having size i and is calculated from [18]

$$C_{D,i} = 0.36 + \frac{24}{\text{Re}_{d,i}} + \frac{5.48}{\text{Re}_{d,i}^{0.573}} \quad and \quad \text{Re}_{d,i} = \frac{\rho_g d_i \left\| \mathbf{u}_g - \mathbf{u}_{d,i} \right\|}{\mu_g}$$
(A.2)

In the numerical implementation, the underscored term of equation (A.1) is treated explicitly and added to the source of the algebraic equation while the double underscored term is treated implicitly with the coefficient  $\sum_{i} A_{i}^{D}$  added to the  $A_{P}$  coefficient of the algebraic equation.

#### REFERENCES

- 1. Bogdanoff, D.W.,"Advanced injection and Mixing techniques for Scramjet Combustors," Journal of Propulsion and Power, vol. 10, no. 2, pp. 183-190, 1994.
- 2. Kay, I.W., Peshke, W. T., and Guile, R. N., Hydrocarbon Fueled Scramjet Combustor Investigations, Journal of Propulsion and Power, vol.8, pp. 507-512,1992.
- 3. Rajasekaran, A. and Babu, V.,"Numerical Simulation of Kerosene Combustion in a Dual Mode Supersonic Combustor," 42nd AIAA/ASME/SAE/ASEE Joint Propulsion Conference and Exhibition, 9-12 July 2006, Sacremento, California, Paper AIAA-2006-5041.
- 4. Burger, M., Klose, G., Rottenkolber, G., Schmehl, R., Giebert, D., Schafer, O., Koch, R., and Wittig, S., A combined Eulerian and Lagrangian Method for Prediction of Evaporating Sprays, Journal of Engineering Gas Turbines and Power, vol. 124, no. 3, pp. 481-488, 2002.
- 5. Schmehl, R., Klose, G., Maier, G., and Wittig, S.,"Efficient Numerical Calculation of Evaporating Sprays in Combustion Chamber Flows," 92<sup>nd</sup> Symposium on Gas Turbine Combustion, Emissions and Alternative Fuels, RTO Meeting Proceedings 14, 1998.
- 6. Hallman, M., Scheurlen, M., and Wittig, S. "Computation of Turbulent Evaporating Sprays: Eulerian versus Lagrangian Approach," Transaction of the ASME, vol. 117, pp.112-119, 1995.
- 7. Wittig, S., Hallmann, M., Scheurlen, M., and Schmehl, R., "A new Eulerian model for turbulent evaporating sprays in recirculating flows," AGARD Meeting on "Fuels and Combustion Technology for advanced Aircraft Engines" (SEE N94-29246 08-25), May 1993.
- 8. Klose, G., Schmehl, R., Meier, R., Maier, G., Koch, R., Wittig, S., Hettel, M., Leuckel, W., and Zarzalis, N., "Evaluation of Advanced Two-Phase Flow and Combustion Models for Predicting Low Emission Combustors," Journal of Engineering for Gas Turbines and Power, vol. 123, pp. 817-823, 2001.
- 9. J.B. Greenberg, I. Silverman, and Y. Tambour, "On the Origin of Spray Sectional Conservation Equations," Combustion and Flame, vol. 93, pp. 90–96, 1993.
- 10. F. Laurent, Modelisation Mathematique et Numerique de la Combustion de Brouillards de Gouttes Polydisperses, Ph.D. Thesis of Universite Claude Bernard, Lyon 1, 2002.
- 11. M. Massot, Modelisation Mathematique des Milieux Reactifs, Habilitation a Diriger des Recherches Thesis of Universite Claude Bernard, Lyon 1, 2003.
- 12. F. Laurent, M. Massot, and P. Villedieu, "Eulerian Multi-Fluid Modelling for the Numerical Simulation of Coalescence in Polydisperse Dense Liquid Sprays," Journal of Computational Physics, vol. 194, pp. 505-543, 2004.
- 13. R.O. Fox, F. Laurent, and M. Massot, "Numerical Simulation of Spray Coalescence in an Eulerian Framework: Direct Quadrature Method of Moments and Multi-fluid Method," Journal of Computational Physics, preprint version, 2007.

- 14. D.P. Brown, E.I Kauppinen, J.K. Jokiniemi, S.G. Rubin, and P. Biswas, "A Method of Moments Based CFD Model for Polydisperse Aerosol Flows with Strong Interphase Mass and Heat Transfer," Computers & Fluids, vol. 35, pp. 762-780, 2006.
- 15. L. Hagessaether, Coalescence and Break-up of Drops and Bubbles, Thesis submitted for the degree of DR. ENG, Norwegian University of science and technology, March 2002.
- 16. Launder, B.E. and Spalding, D.B., "The Numerical Computation of Turbulent Flows," Comp. Methods Appl. Mech. Eng., vol. 3, pp. 269-289, 1974.
- 17. Melville, W.K. and Bray, K.N.C, "A model of the two phase turbulent Jet," International Journal of Heat and Mass Transfer, vol. 22, pp. 647-656, 1979.
- 18. Krämer, M., Untersuchungen zum Bewegungsverhalten von Tropfen in turbulenter Strömung im Hinblick auf Verbrennungsvorgänge, Dissertation, Institut für Feuerungstechnik, Universität Karlsruhe (T.H.), 1988.
- 19. Luo, H., Svendsen, H. "Theoretical model for drop and bubble breakup in turbulent dispersions", *AiChE journal*, vol.42, no. 5, pp. 1225-1233, 1996.
- 20. Tsouris, C., Tavlarides, L.L., "Breakage and Coalescence Models for Drops in Turbulent Dispersions", *AIChE Journal*, vol. 40, no. 3, pp. 395-406, 1994.
- 21. Hassanizadeh M., Gray W.G. "General Conservation Equations for Multi-Phase Systems, I. Averaging procedure", Adv. Water Resources, vol. 2, pp. 131-190, 1979.
- 22. Hassanizadeh M., Gray W.G., "General Conservation Equations for Multi-Phase Systems: 2, Mass, Momenta, Energy and Entropy Equations", Adv. Water Res., vol. 2, pp. 191-202, 1979.
- 23. Godsave, G.A.E., Studies of the Combustion of Drops in a Fuel Spray the Burning of Drops of Fuel, Prococeedings of the 4<sup>th</sup> International Symposium on Combustion, pp. 818-830, 1953.
- 24. Spalding, D.B., The Combustion of Liquid Fuels, Prococeedings of the 4<sup>th</sup> International Symposium on Combustion, pp. 847-864, 1953.
- 25. Hubbard, G.L., Denny, V.E., Mils, A.F., Droplet Evaporation: Effects of Transients and Variable Properties, International Journal of Heat and Mass Transfer, vol. 18, pp. 1003-1008, 1975.
- 26. Aggarawal, S.K., Tong, A.Y., and Sirignano, W.A., A Comparison of Vaproization Models in Spray Calculations. AIAA Journal, vol. 22, no. 10, pp. 1448-1457, 1984.
- 27. Chen, X.Q. and Pereira, J.C.F., Computation of Turbulent Evaporating Sprays with well-Specified Measurements: A Sensitivity Study on Droplet Properties, International Journal of Heat and Mass Transfer, vol. 39, no. 3, pp. 441-454, 1996.
- 28. Schmehl, R., Theory and Application of Droplet Evaporation Models, Institut Fur Thermische Stromungsmaschinen.
- 29. Sazhin, S.S. and Abdelghaffar, W.A., New Approaches to Numerical Modeling of Droplet Transient Heating and Evaporation, International Journal of Heat and Mass Transfer, vol. 48, pp. 4215-4228, 2005.
- 30. Bertoli, C. and Migliaccio, M., A Finite Conductivity Model for Diesel Spray Evaporation Computations, International Journal of Heat and Fluid Flow, vol. 20, pp. 552-561, 1999.
- 31. Talley, D.G. and Yao, S.C., A Semi-empirical Approach to Thermal and Composition Transients Inside Vaporizing Fuel Droplets, Prococeedings of the 21<sup>st</sup> International Symposium on Combustion, The Combustion Institute, pp. 609-616, 1986.

- 32. Jin, J.D. and Borman, G.L., A Model for Multi-component Droplet Vaporization at High Ambient Pressures, Combustion Emission and Analysis, P-162, pp. 213-223, SAE, Inc., 1985.
- 33. Sazhin, S.S., Advanced Models of Fuel Droplet Heating and Evaporation, Progress in Energy and Combustion Science, vol. 32, pp. 162-214, 2006.
- 34. Abramzon, B. and Sirignano, W.A., Droplet Vaporization Model for Spray Combustion Calculations. International Journal of Heat and Mass Transfer, vol. 32, no. 9 pp. 1605-1618, 1989.
- 35. Miller, R.S., Harstad, K., and Bellan, J., Evaluation of Equilibrium and Non-equilibrium Evaporation Models for Many-Droplet Gas-Liquid Flow Simulations. International Journal of Multiphase Flow, vol. 24, pp. 1025–1055, 1998.
- 36. Aggarwal, S.K. and Peng, F.,"A review of Droplet Dynamics and Vaporization Modeling for Engineering Calculations," ASME Journal of Engineering for Gas Turbine and Power, vol. 117, pp. 453-461, 1995.
- 37. Faeth, G.M., "Evaporation and Combustion of Sprays," Prog. Energy Combust. Sci., vol. 9, pp. 1-76, 1983.
- 38. Frössling, N., "Über die Verdunstung fallender Tropfen," Gerlands Beiträge zur Geophysik, vol. 52, pp. 170-215, 1938.
- 39. Darwish, M., Moukalled, F., and., Sekar, B., A Unified Formulation of the Segregated Class of Algorithms for Multi-phase Flow at All Speeds, *Numerical Heat Transfer*, Part B, vol. 40, no. 2, pp. 99-137, 2001.
- 40. Lo, S.M., "Multiphase Flow Model in harwell-FLOW#D Computer Code", Report AEA-InTec-0062, 1990.
- 41. Spalding, D.B. and Markatos, N.C., "Computer Simulation of Multi-Phase Flows: A Course of Lectures and Computer Workshops", Report CFD/83/4, Mech. Eng., Imperical College, London, 1983.
- 42. Hancox, W.T. and Banerjee, S.,"Numerical Standards for Flow Boiling Analysis," Nuclear Science & Engineering, vol. 64, p. 106, 1977.
- 43. F. Moukalled and M. Darwish," Supersonic Turbulent Fuel-Air Mixing and Evaporation," Proceedings of the Twelfth IASTED International Conference on Applied Simulation and Modelling, Sept. 3-5, Marbella, Spain, pp. 1-6, 2003.
- 44. Patankar, S.V., Numerical Heat Transfer and Fluid Flow, Hemisphere, N.Y., 1981.
- 45. Moukalled, F. and Darwish, M.," A Unified Formulation of the Segregated Class of Algorithms for Fluid Flow at All Speeds," Numerical Heat Transfer, Part B, vol. 37, no. 1, pp. 103-139, 2000.
- 46. E. Gharaibah, M. Brandt, W. Polifke: A Numerical Model of Dispersed Two Phase Flow in Aerated Stirred Vessels Based on Presumed Shape Number Density Functions, Heidelberg, Springer-Verlag Berlin Heidelberg, pp. 295-305, 2004.
- 47. CFX-5.7 Solver manual.
- 48. G.H. Yeoha, J.Y. Tub: Population Balance Modeling for Bubbly Flows with Heat and Mass Transfer, Chemical Engineering Science, vol. 59, pp. 3125 3139, 2004.
- 49. I. P. Jones, P. W. Guilbert, M. P. Owens, I. S. Hamill, C. A. Montavon, J.M. T Penrose, and B. Prast, The Use of Coupled solvers for Complex Multi-Phase and Reacting Flows, Proceedings of the Third International Conference on CFD in the Minerals and Process Industries CSIRO, Melbourne, pp. 13-20, 2003.

- 50. Z. Sha, Combining Population Balance with Multiphase CFD, Lappeenranta University of Technology, MAHA project, November 2003.
- 51. T. Frank, P. J. Zwart, J.-M. Shi, E. Krepper, D. Lucas, and U. Rohde, Inhomogeneous MUSIG Model- a Population Balance Approach for Polydispersed Bubbly Flows, International conference- Nuclear Energy for New Europe, Bled, Slovenia, 2005.
- 52. J.-M. Shi, P.J. Zwart, T. Frank, U. Rohde, H.-M. Prasser, Development of a Multiple Velocity Multiple Size Group Model for Polydispersed Multiphase Flows, pp. 21-26, Annual Report 2004, Forschungszentrum Rossendorf, Germany, 2004.
- 53. M. Sommerfeld and H. Qiu, Experimental Studies of Spray Evaporation in Turbulent Flow, International Journal of Heat and Fluid Flow, vol. 19, pp. 10-22, 1998.
- 54. X. Q. Chen and J. C. F. Periera, Prediction of Evaporating Spray in Anisotropically Turbulent Gas Flow, Numerical Heat Transfer, Part A, vol. 27, pp. 143-162, 1995.
- 55. M. A. Founti, D. I. Katsourinis, and D. I. Kolaitis, Turbulent Sprays Evaporating under Stabilized Cool Flame Conditions: Assessment of Two CFD Approaches, Numerical Heat Transfer, Part B, vol. 52, pp. 51-68, 2007.

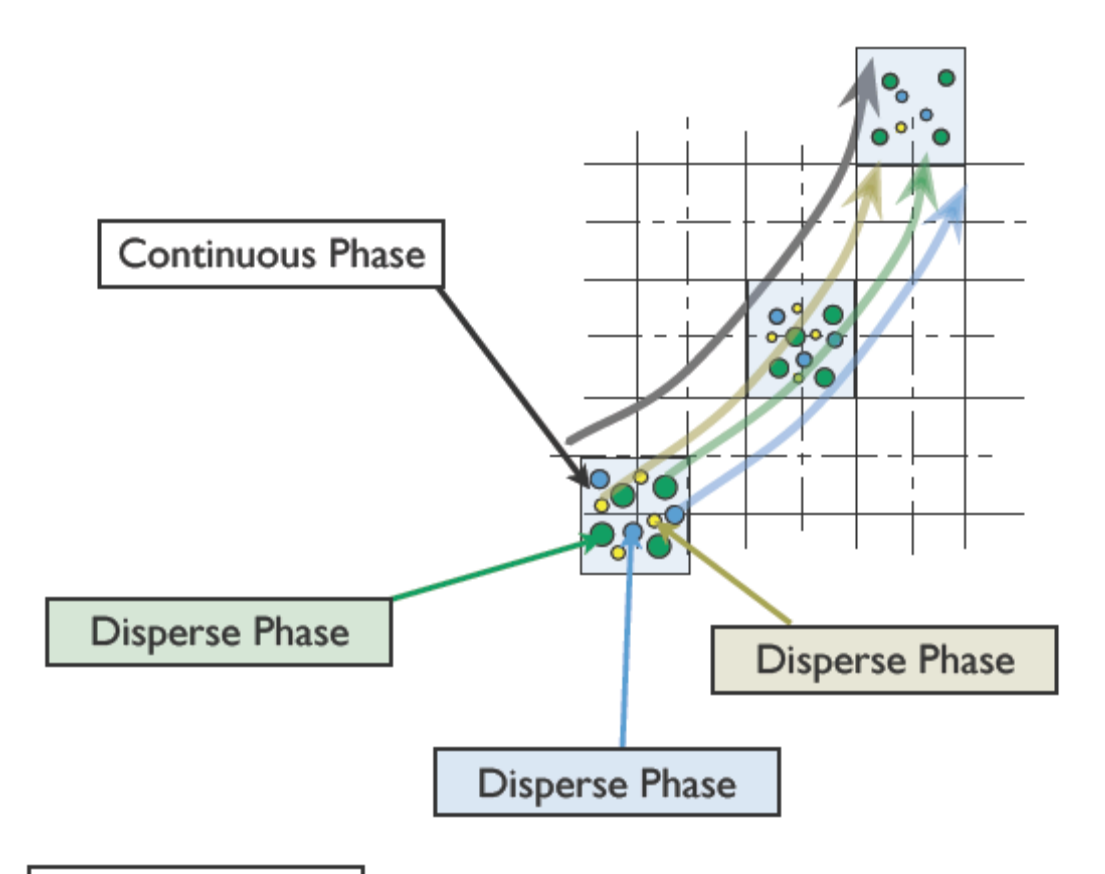
## FIGURE CAPTIONS

- Figure 1 Schematic of the full multiphase approach.
- Figure 2 Schematic of the MUSIG approach.
- Figure 3 Schematic of the H-MUSIG approach.
- Figure 4 Comparison of measured and computed radial profiles for (a) the gas mean axial velocity and (b) the droplet mean axial velocity.
- Figure 5 Comparison of measured and computed radial profiles for (a) the gas and (b) droplet turbulent kinetic energy.
- Figure 6 Physical domain for (a) streamwise injection in a rectangular duct, (b) cross-stream injection in a rectangular duct, and (c) an illustrative grid.
- Figure 7 Velocity fields predicted by the full multiphase (a,b,c, in increasing droplet size), the H-MUSIG (d, e, in increasing Sauter diameter) and the MUSIG (f) methods for streamwise injection in a subsonic flow field (M<sub>in</sub>=0.2).
- Figure 8 Comparison of (a) gas volume fraction, (b) vapor mass fraction, (c) gas density, and (d) gas turbulent viscosity contours generated using the Full multiphase method with 5 droplet phases (solid line), the H-MUSIG method with 2 droplet phases and 5 size groups per phase (dashed lines), and the MUSIG method with 10 size groups (dotted lines) (M<sub>in</sub>=0.2, streamwise injection).
- Figure 9 Comparison of (a) u-velocity, (b) temperature, (c) pressure, and (d) vapor mass fraction profiles across the domain at x=0.5m generated using the full multi-phase, MUSIG, and H-MUSIG methods ( $M_{in}=0.2$ , streamwise injection).

- Figure 10 Comparison of the average droplet (a) mass density, (b) turbulent kinetic energy, (c) temperature, and (d) relative axial velocity in the streamwise direction generated using the full multi-phase, MUSIG, and H-MUSIG methods (M<sub>in</sub>=0.2, streamwise injection).
- Figure 11 Velocity fields predicted by the full multiphase (a,b,c, in increasing droplet size), the H-MUSIG (d, e, in increasing Sauter diameter) and the MUSIG (f) methods for streamwise injection in a supersonic flow field ( $M_{in}$ =2).
- Figure 12 Comparison of (a) gas volume fraction, (b) vapor mass fraction, (c) gas density, and (d) gas turbulent viscosity contours generated using the Full multiphase method with 5 droplet phases (solid line), the H-MUSIG method with 2 droplet phases and 5 size groups per phase (dashed lines), and the MUSIG method with 10 size groups (dotted lines) (M<sub>in</sub>=2, streamwise injection).
- Figure 13 Comparison of (a) u-velocity, (b) temperature, (c) pressure, and (d) vapor mass fraction profiles across the domain at x=0.5m generated using the full multi-phase, MUSIG, and H-MUSIG methods ( $M_{in}=2$ , streamwise injection).
- Figure 14 Comparison of the average droplet (a) mass density, (b) turbulent kinetic energy, (c) temperature, and (d) relative axial velocity in the streamwise direction generated using the full multi-phase, MUSIG, and H-MUSIG methods (M<sub>in</sub>=2, streamwise injection).
- Figure 15 Velocity fields predicted by the full multiphase (a,b,c, in increasing droplet size), the H-MUSIG with 2 droplet phases and 5 size groups per phase (d, e, in increasing Sauter diameter) and the MUSIG (f) methods for cross stream injection in a subsonic flow field (M<sub>in</sub>=0.2).

- Figure 16 Velocity fields predicted by the H-MUSIG with 5 droplet phases (2 size groups per phase) in increasing Sauter diameter for the first (a), third (b), and fifth (c) phases, for cross stream injection in a subsonic flow field ( $M_{in}$ =0.2).
- Figure 17 Comparison of (a) gas volume fraction, (b) vapor mass fraction, (c) gas density, and (d) gas turbulent viscosity contours generated using the Full multiphase method with 5 droplet phases (solid line), the H-MUSIG method with 5 droplet phases and 2 size groups per phase (dash-dotted lines), the H-MUSIG method with 2 droplet phases and 5 size groups per phase (dashed lines), and the MUSIG method with 10 size groups (dotted lines) (M<sub>in</sub>=0.2, cross stream injection).
- Figure 18 Comparison of (a) u-velocity, (b) temperature, (c) pressure, and (d) vapor mass fraction profiles across the domain at x=0.6m generated using the full multi-phase, MUSIG, and H-MUSIG methods (M<sub>in</sub>=0.2, cross stream injection).
- Figure 19 Comparison of the average droplet (a) mass density, (b) turbulent kinetic energy, (c) temperature, and (d) relative axial velocity in the streamwise direction generated using the full multi-phase, MUSIG, and H-MUSIG methods (M<sub>in</sub>=0.2, cross stream injection).
- Figure 20 Velocity fields predicted by the full multiphase (a,b,c, in increasing droplet size), the H-MUSIG (d, e, in increasing Sauter diameter) and the MUSIG (f) methods for cross stream injection in a supersonic flow field ( $M_{in}$ =2).
- Figure 21 Comparison of (a) gas volume fraction, (b) vapor mass fraction, (c) gas density, and (d) gas turbulent viscosity contours generated using the Full multiphase method with 5 droplet phases (solid line), the H-MUSIG method with 2 droplet phases and 5 size groups per phase (dashed lines), and the MUSIG method with 10 size groups (dotted lines) (M<sub>in</sub>=2, cross stream injection).

- Figure 22 Comparison of (a) u-velocity, (b) temperature, (c) pressure, and (d) vapor mass fraction profiles across the domain at x=0.6m generated using the full multi-phase, MUSIG, and H-MUSIG methods ( $M_{in}=2$ , cross stream injection).
- Figure 23 Comparison of the average droplet (a) mass density, (b) turbulent kinetic energy, (c) temperature, and (d) relative axial velocity in the streamwise direction generated using the full multi-phase, MUSIG, and H-MUSIG methods (M<sub>in</sub>=2, cross stream injection).



## Continuous Phase

Momentum Equation Continuity Equation Energy Equation Species Equations

# Disperse Phase

Momentum Equation Continuity Equation Energy Equation Droplet Equation

# Disperse Phase

Momentum Equation Continuity Equation Energy Equation Droplet Equation

## Disperse Phase

Momentum Equation
Continuity Equation
Energy Equation
Droplet Equation

Figure 1 Schematic of the full multiphase approach.

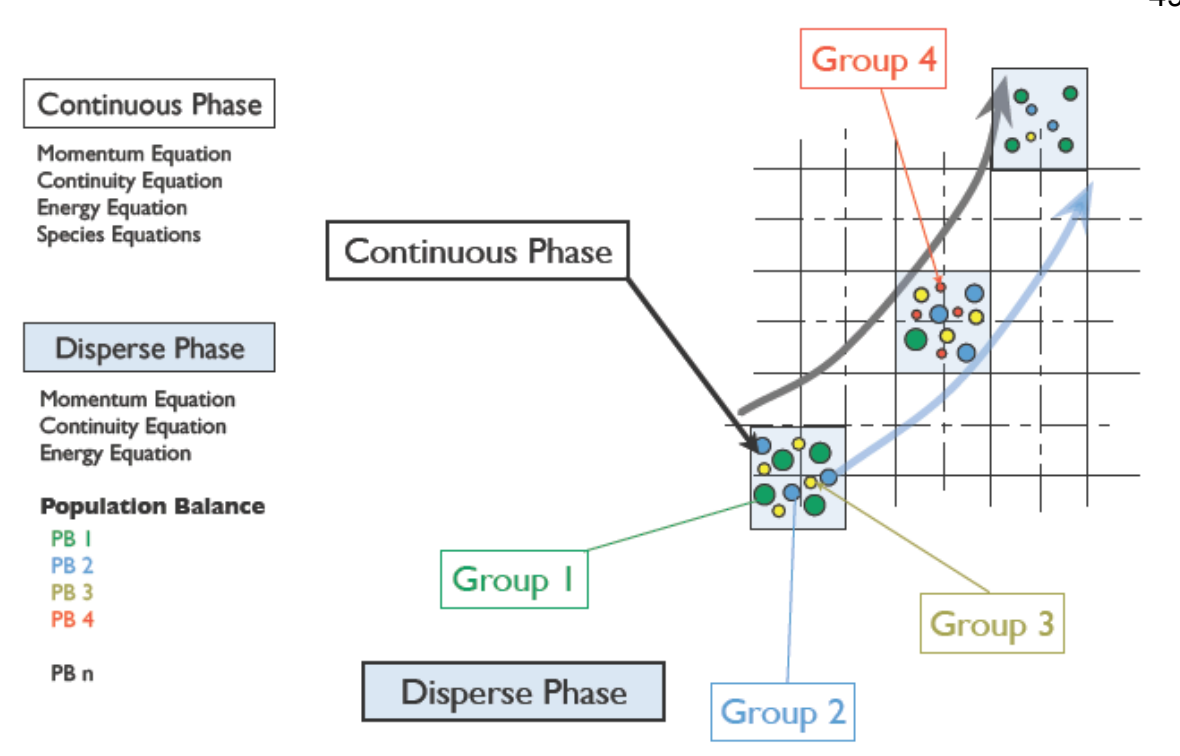


Figure 2 Schematic of the MUSIG approach.

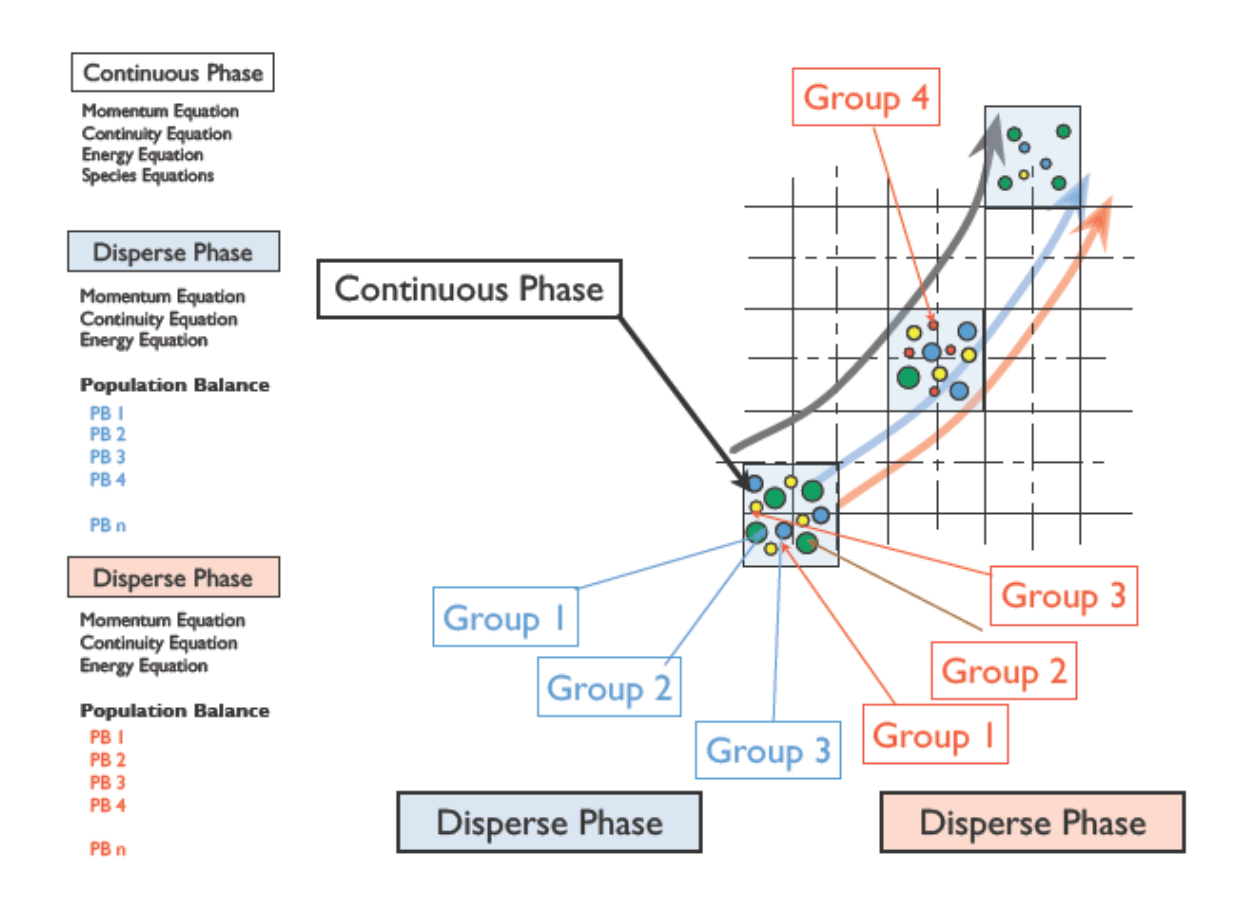


Figure 3 Schematic of the H-MUSIG approach.

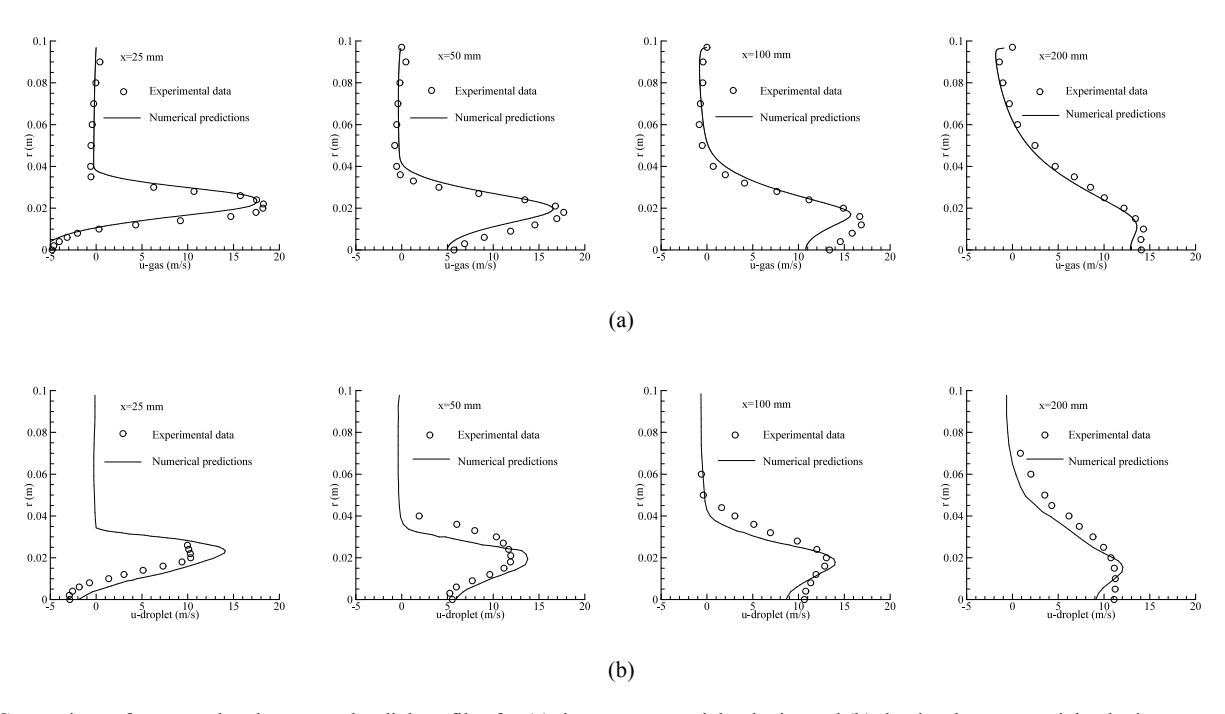


Figure 4 Comparison of measured and computed radial profiles for (a) the gas mean axial velocity and (b) the droplet mean axial velocity.



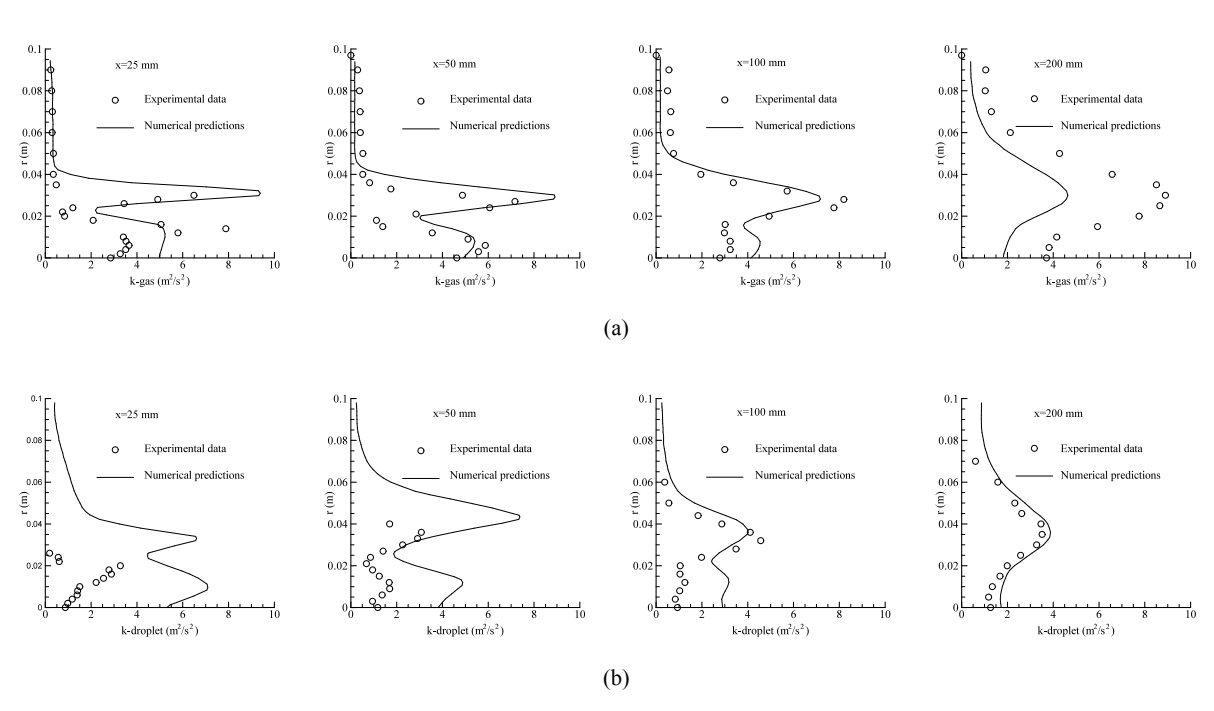


Figure 5 Comparison of measured and computed radial profiles for (a) the gas and (b) droplet turbulent kinetic energy.

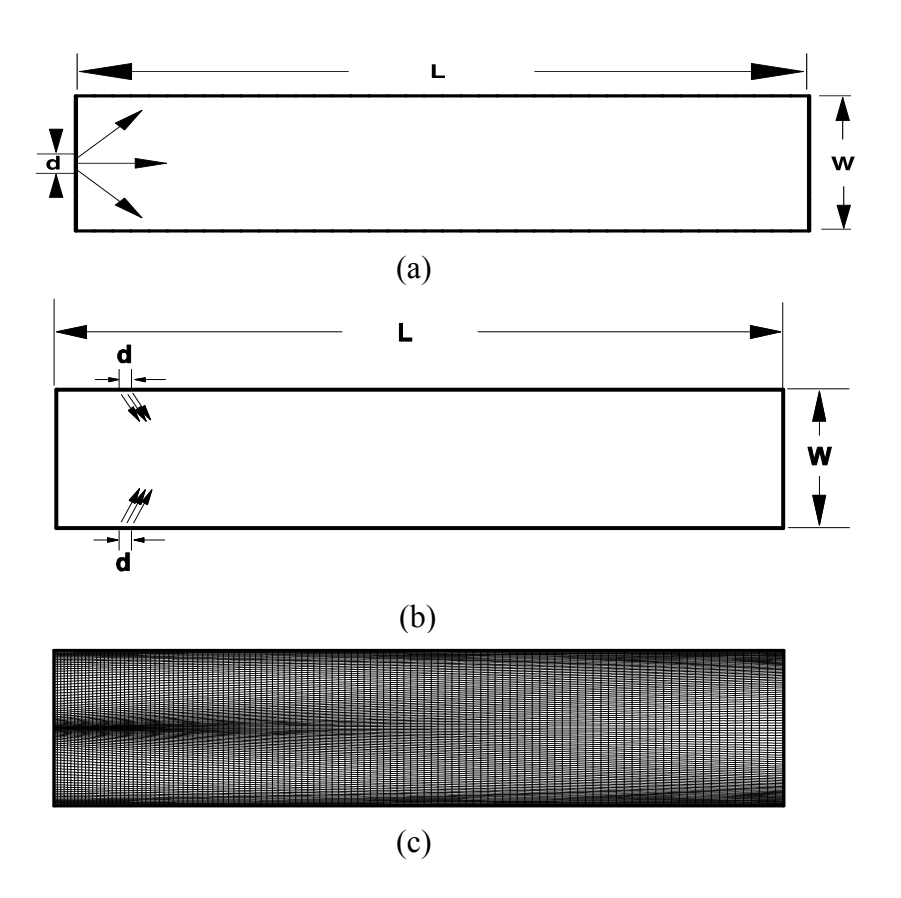


Figure 6 Physical domain for (a) streamwise injection in a rectangular duct, (b) cross-stream injection in a rectangular duct, and (c) an illustrative grid.

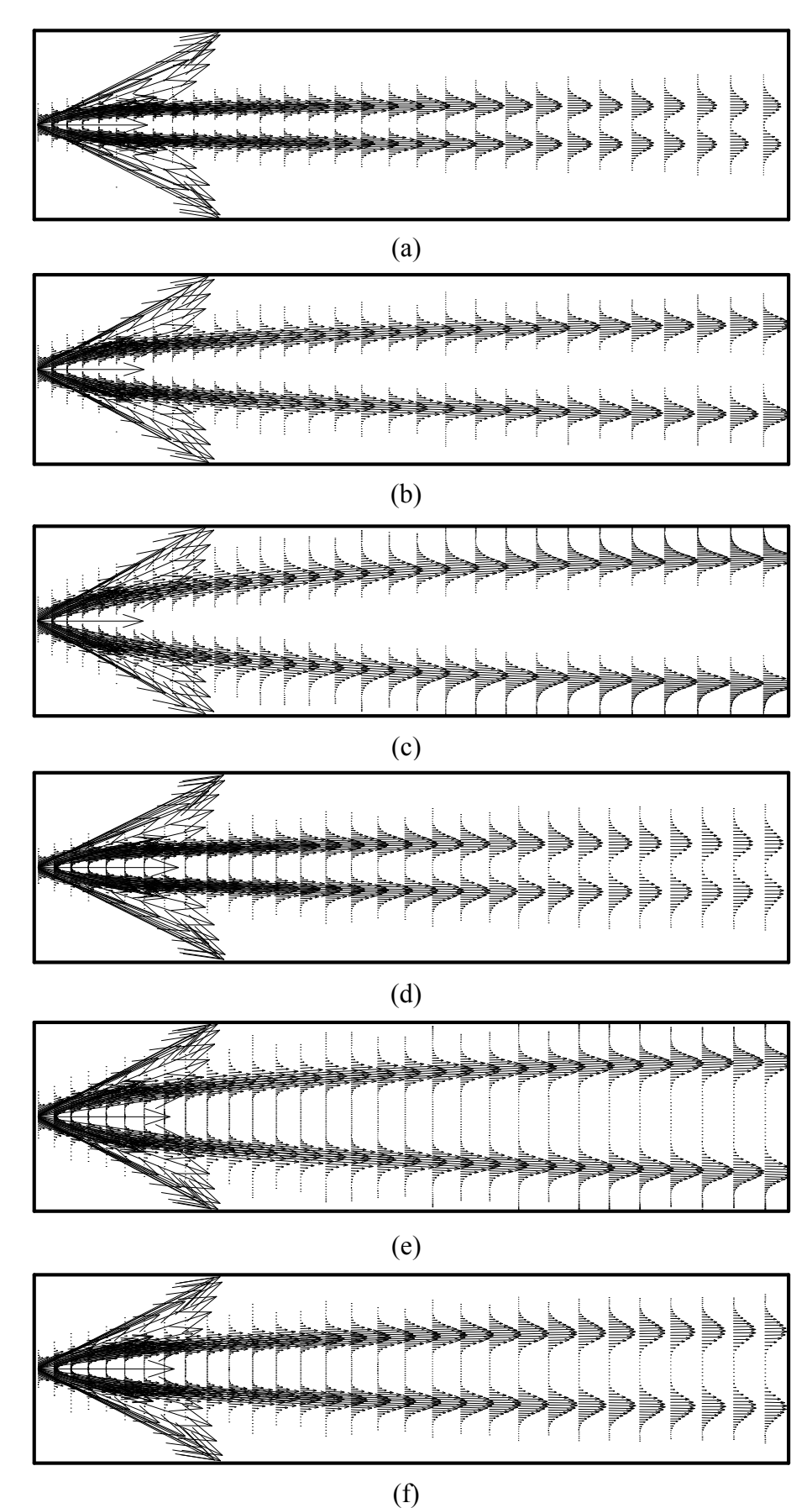


Figure 7 Velocity fields predicted by the full multiphase (a,b,c, in increasing droplet size), the H-MUSIG (d, e, in increasing Sauter diameter) and the MUSIG (f) methods for streamwise injection in a subsonic flow field ( $M_{in}$ =0.2).

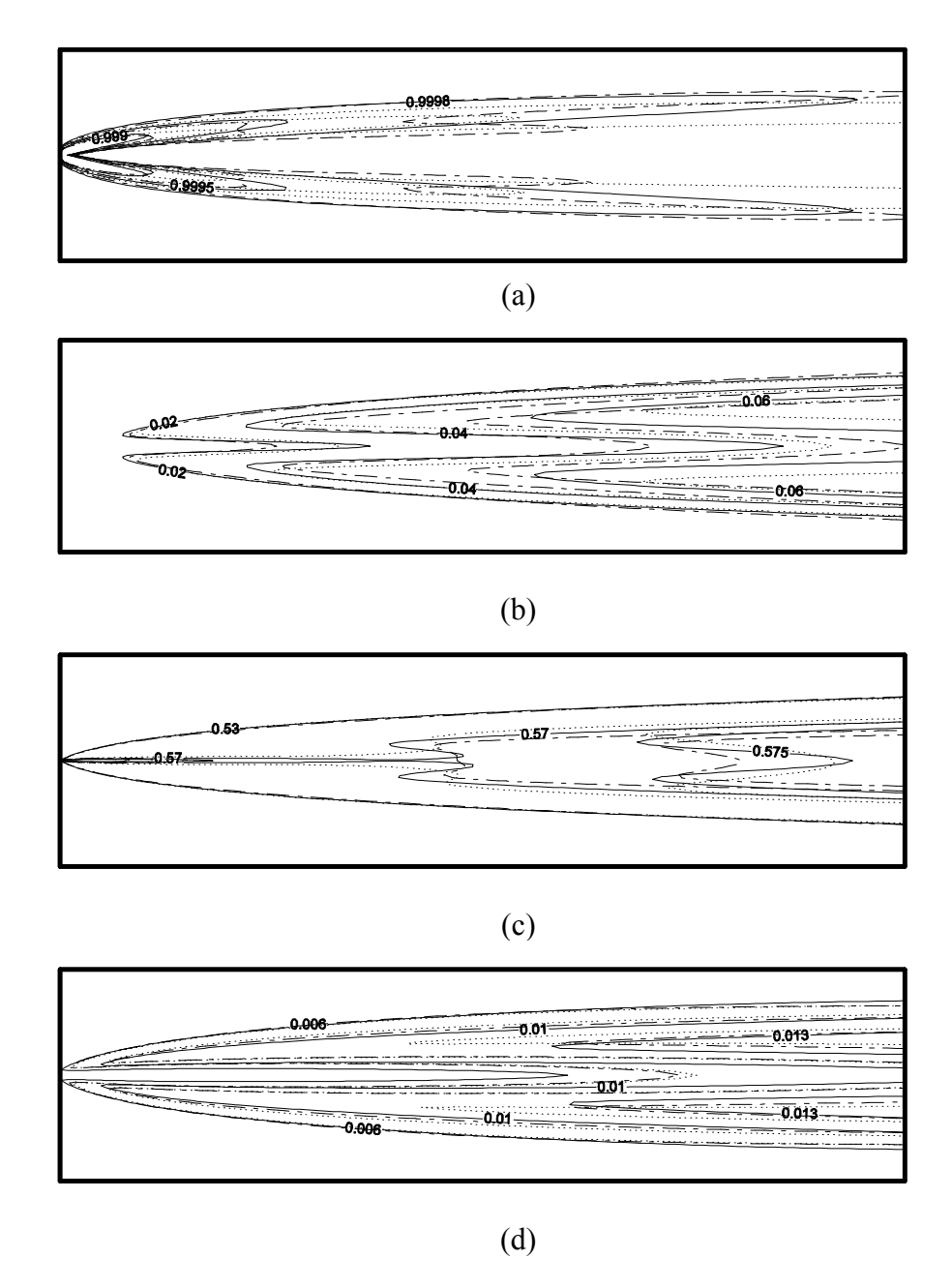


Figure 8 Comparison of (a) gas volume fraction, (b) vapor mass fraction, (c) gas density, and (d) gas turbulent viscosity contours generated using the Full multiphase method with 5 droplet phases (solid line), the H-MUSIG method with 2 droplet phases and 5 size groups per phase (dashed lines), and the MUSIG method with 10 size groups (dotted lines) ( $M_{in}$ =0.2, streamwise injection).

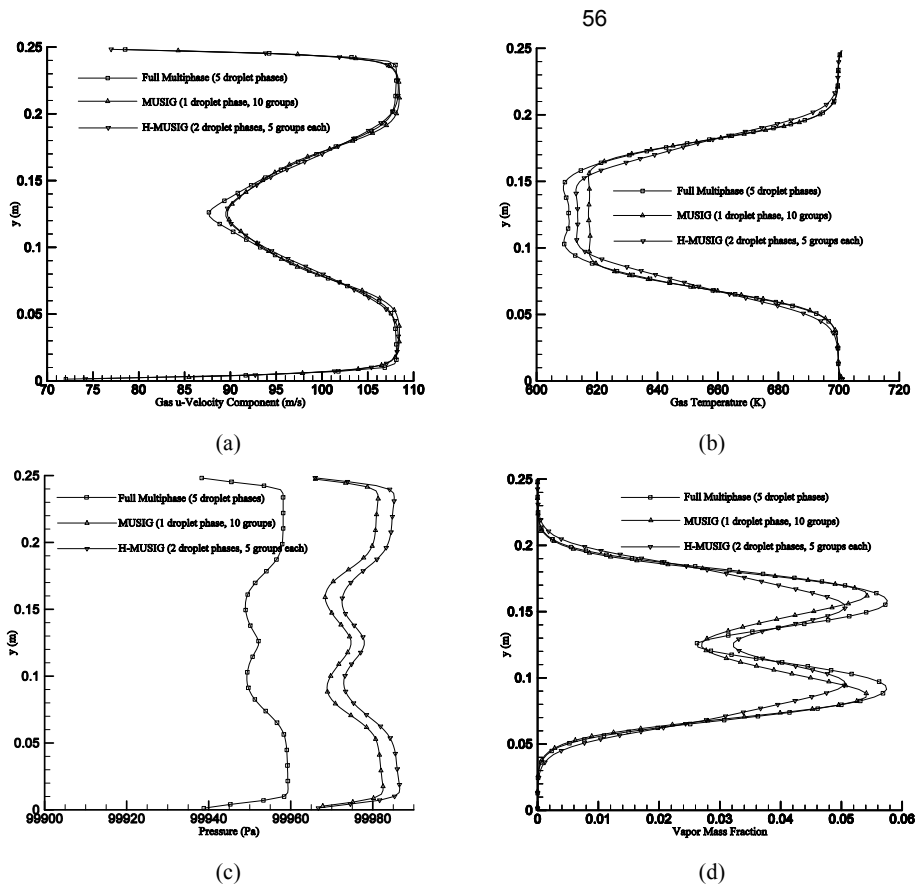


Figure 9 Comparison of (a) u-velocity, (b) temperature, (c) pressure, and (d) vapor mass fraction profiles across the domain at x=0.5m generated using the full multi-phase, MUSIG, and H-MUSIG methods ( $M_{in}=0.2$ , streamwise injection).

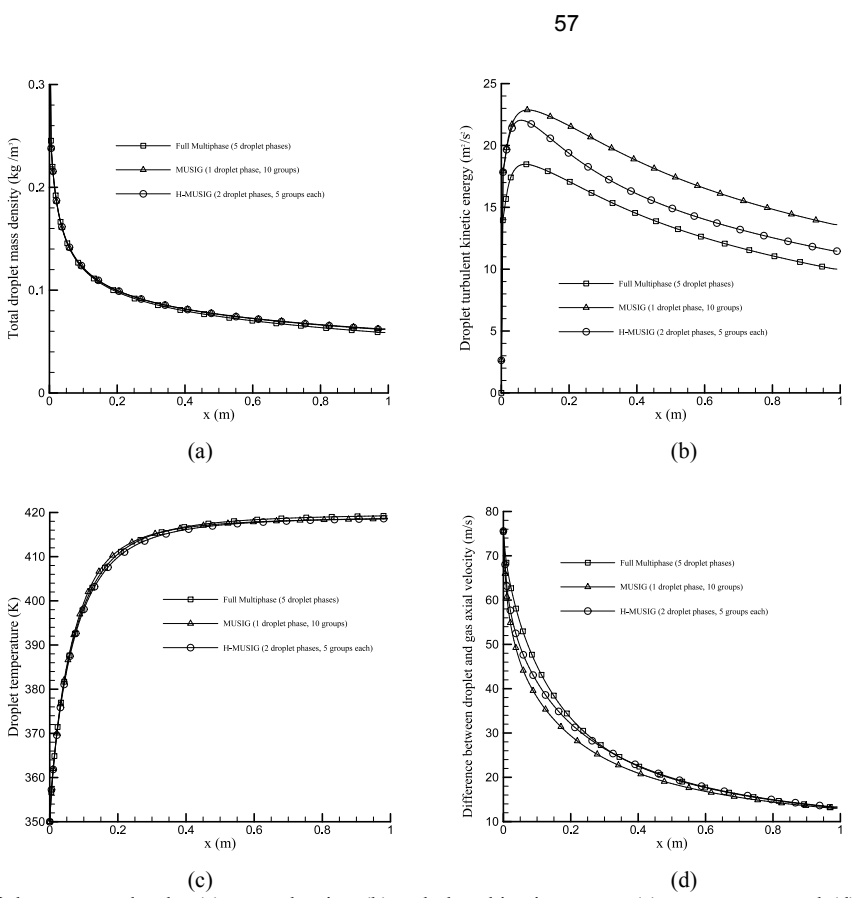


Figure 10 Comparison of the average droplet (a) mass density, (b) turbulent kinetic energy, (c) temperature, and (d) relative axial velocity in the streamwise direction generated using the full multi-phase, MUSIG, and H-MUSIG methods ( $M_{in}$ =0.2, streamwise injection).

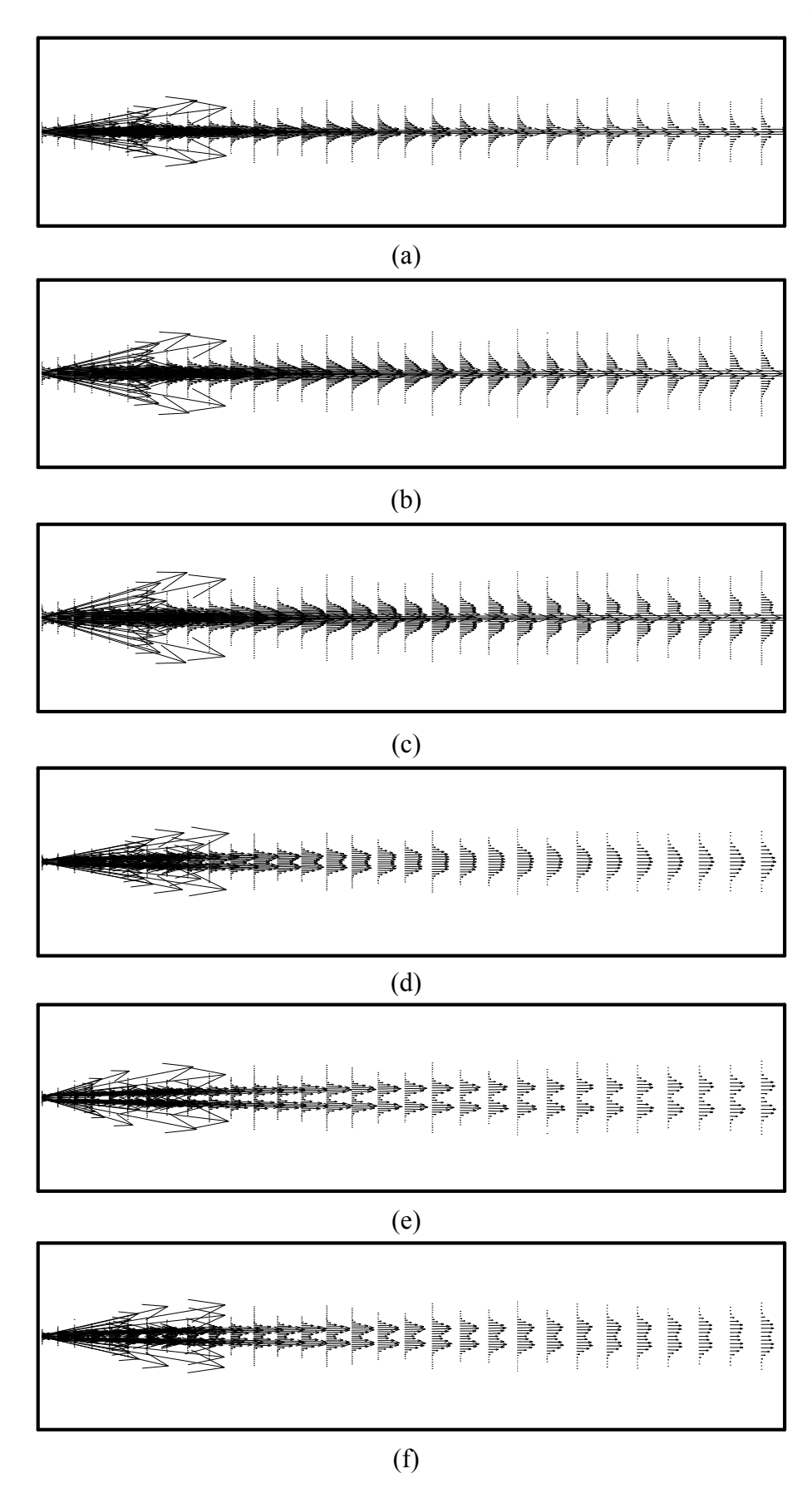


Figure 11 Velocity fields predicted by the full multiphase (a,b,c, in increasing droplet size), the H-MUSIG (d, e, in increasing Sauter diameter) and the MUSIG (f) methods for streamwise injection in a supersonic flow field ( $M_{in}$ =2).

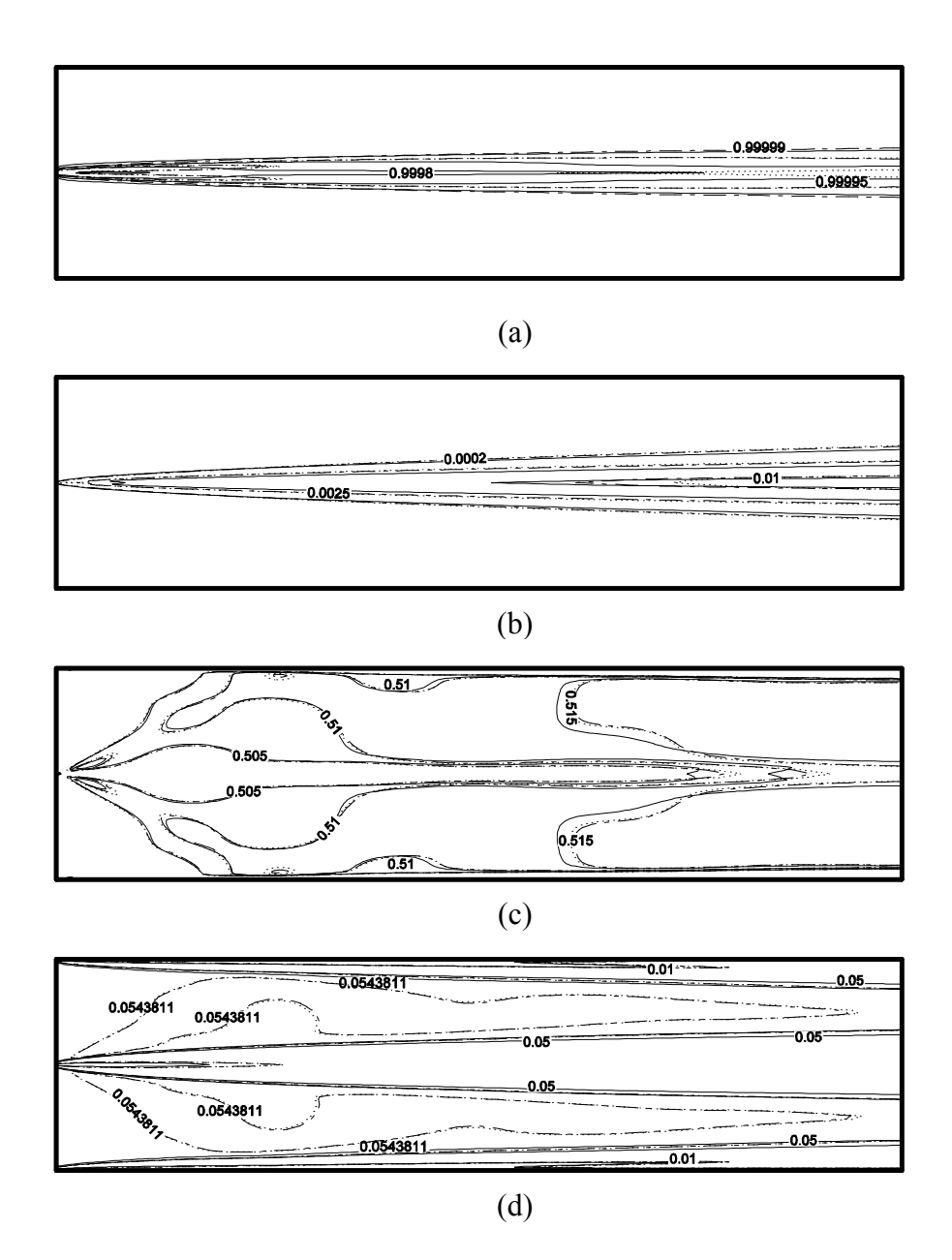
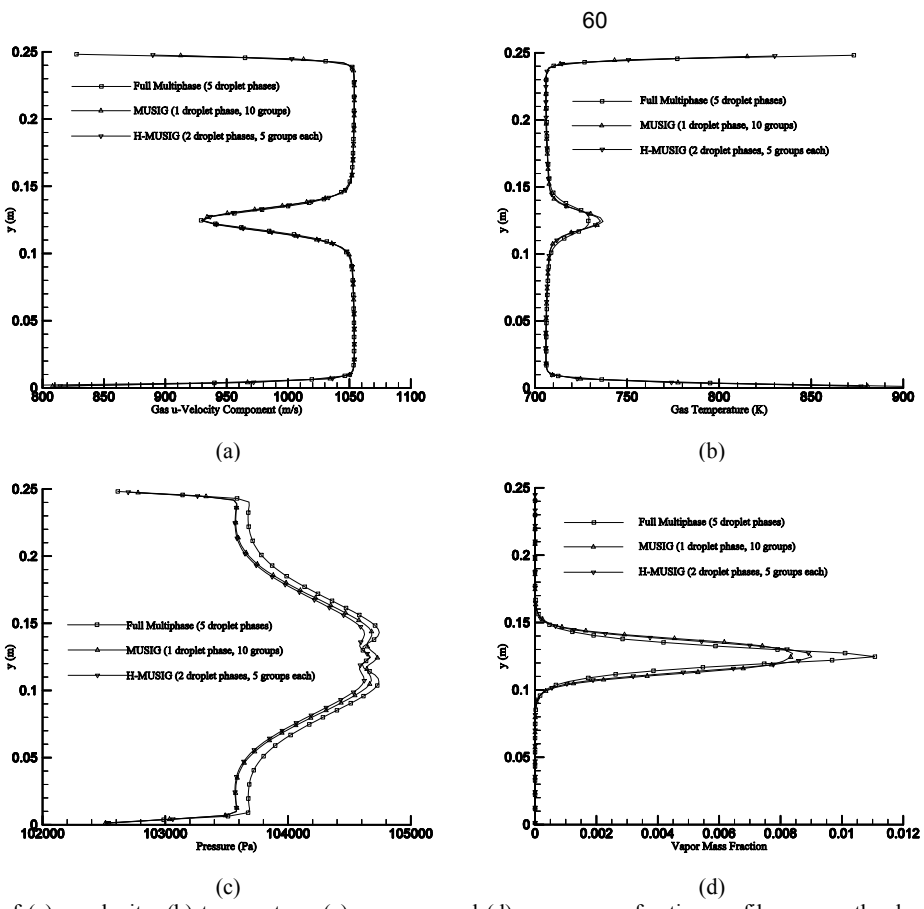
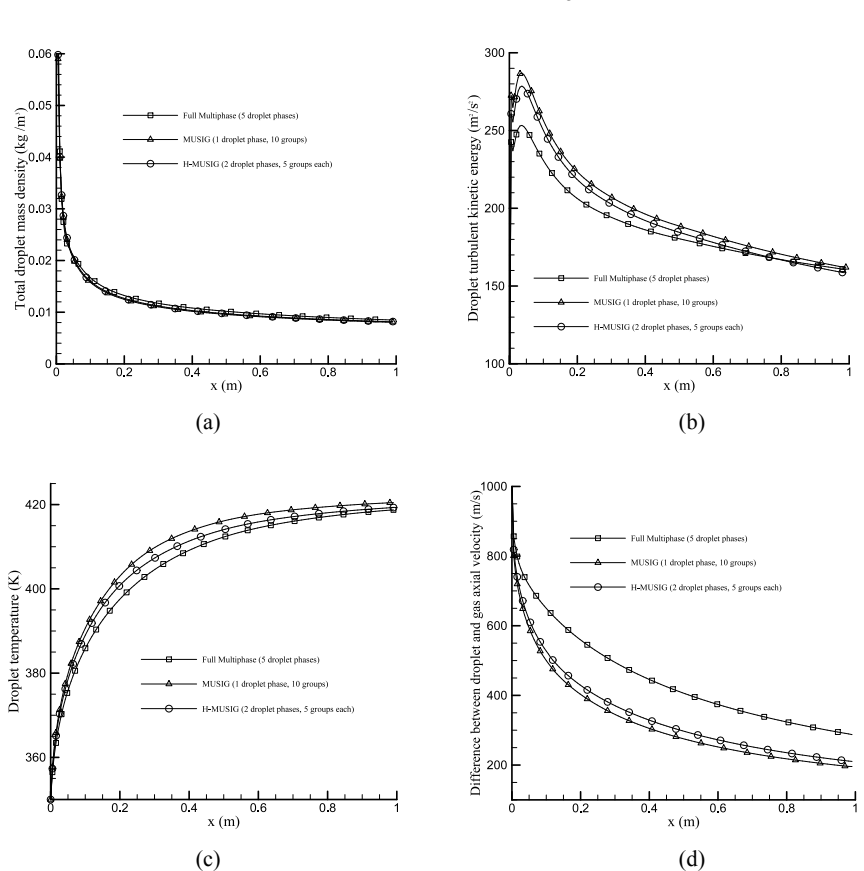


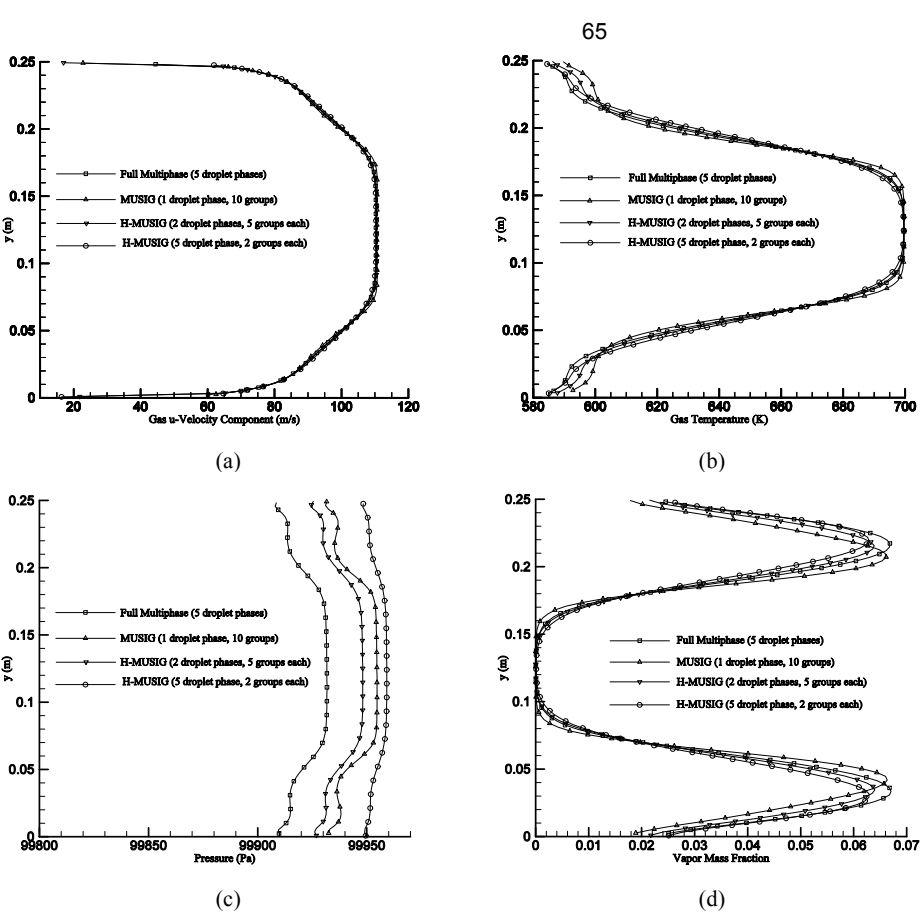
Figure 12 Comparison of (a) gas volume fraction, (b) vapor mass fraction, (c) gas density, and (d) gas turbulent viscosity contours generated using the Full multiphase method with 5 droplet phases (solid line), the H-MUSIG method with 2 droplet phases and 5 size groups per phase (dashed lines), and the MUSIG method with 10 size groups (dotted lines) ( $M_{in}$ =2, streamwise injection).



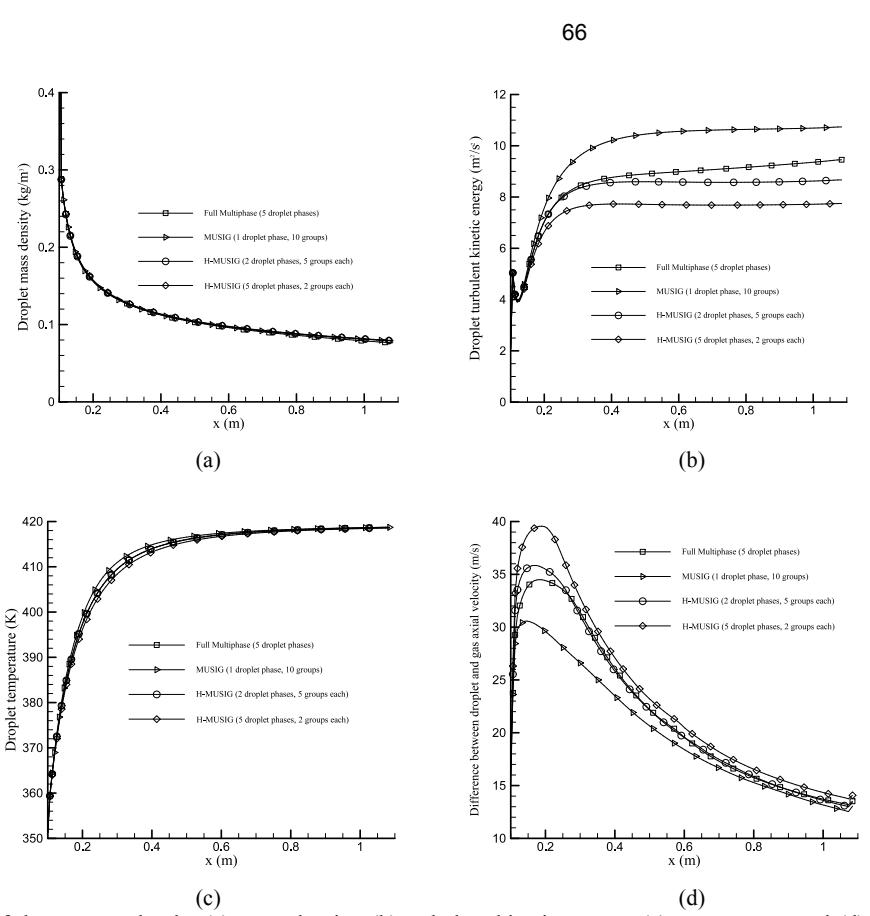
(c) (d) Figure 13 Comparison of (a) u-velocity, (b) temperature, (c) pressure, and (d) vapor mass fraction profiles across the domain at x=0.5m generated using the full multi-phase, MUSIG, and H-MUSIG methods ( $M_{in}=2$ , streamwise injection).



(c) (d)
Figure 14 Comparison of the average droplet (a) mass density, (b) turbulent kinetic energy, (c) temperature, and (d) relative axial velocity in the streamwise direction generated using the full multi-phase, MUSIG, and H-MUSIG methods (M<sub>in</sub>=2, streamwise injection).



(c) (d) Figure 18 Comparison of (a) u-velocity, (b) temperature, (c) pressure, and (d) vapor mass fraction profiles across the domain at x=0.6m generated using the full multi-phase, MUSIG, and H-MUSIG methods ( $M_{in}=0.2$ , cross stream injection).



(c) (d) Figure 19 Comparison of the average droplet (a) mass density, (b) turbulent kinetic energy, (c) temperature, and (d) relative axial velocity in the streamwise direction generated using the full multi-phase, MUSIG, and H-MUSIG methods ( $M_{in}$ =0.2, cross stream injection).

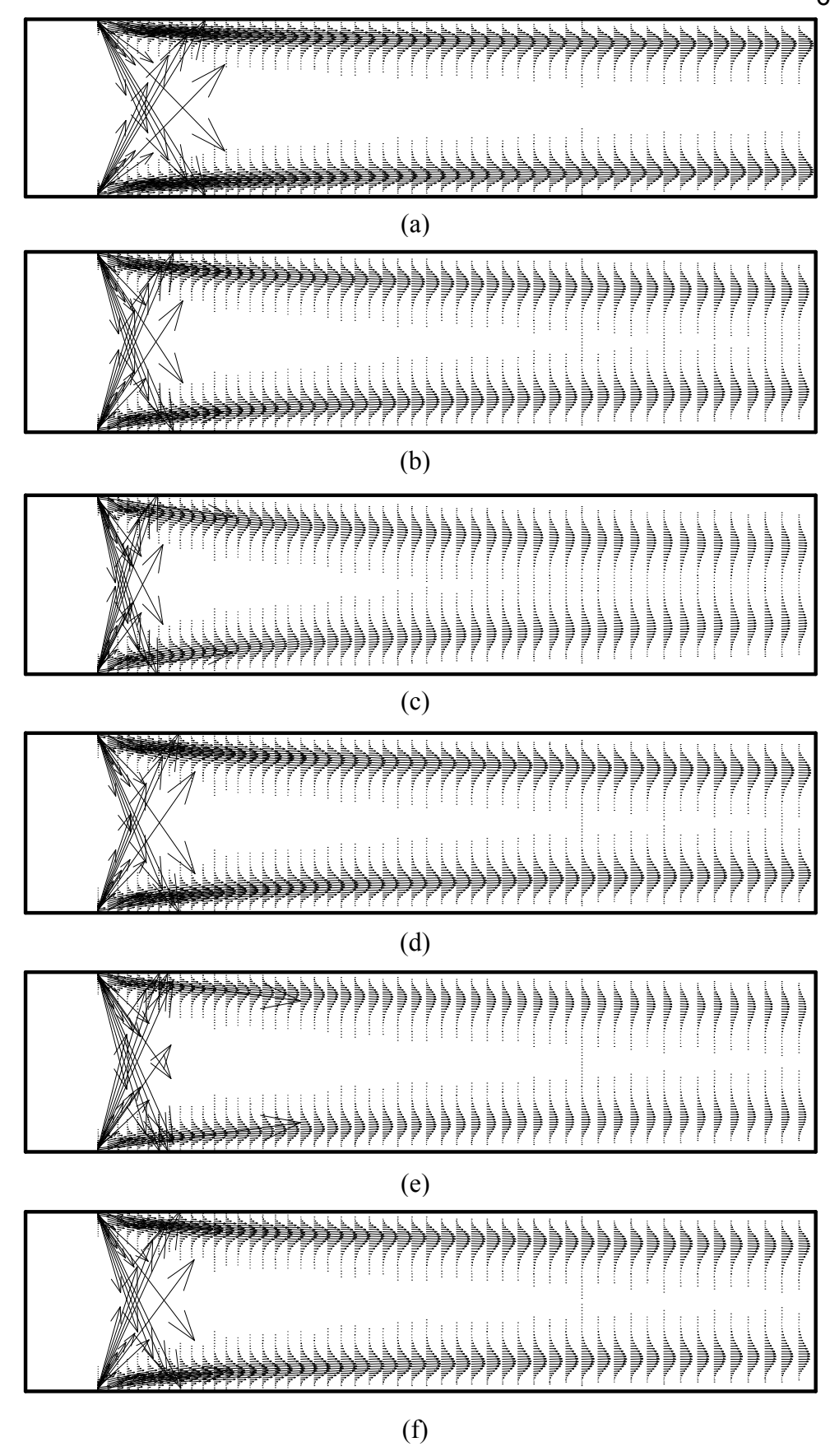


Figure 20 Velocity fields predicted by the full multiphase (a,b,c, in increasing droplet size), the H-MUSIG (d, e, in increasing Sauter diameter) and the MUSIG (f) methods for cross stream injection in a supersonic flow field ( $M_{in}$ =2).

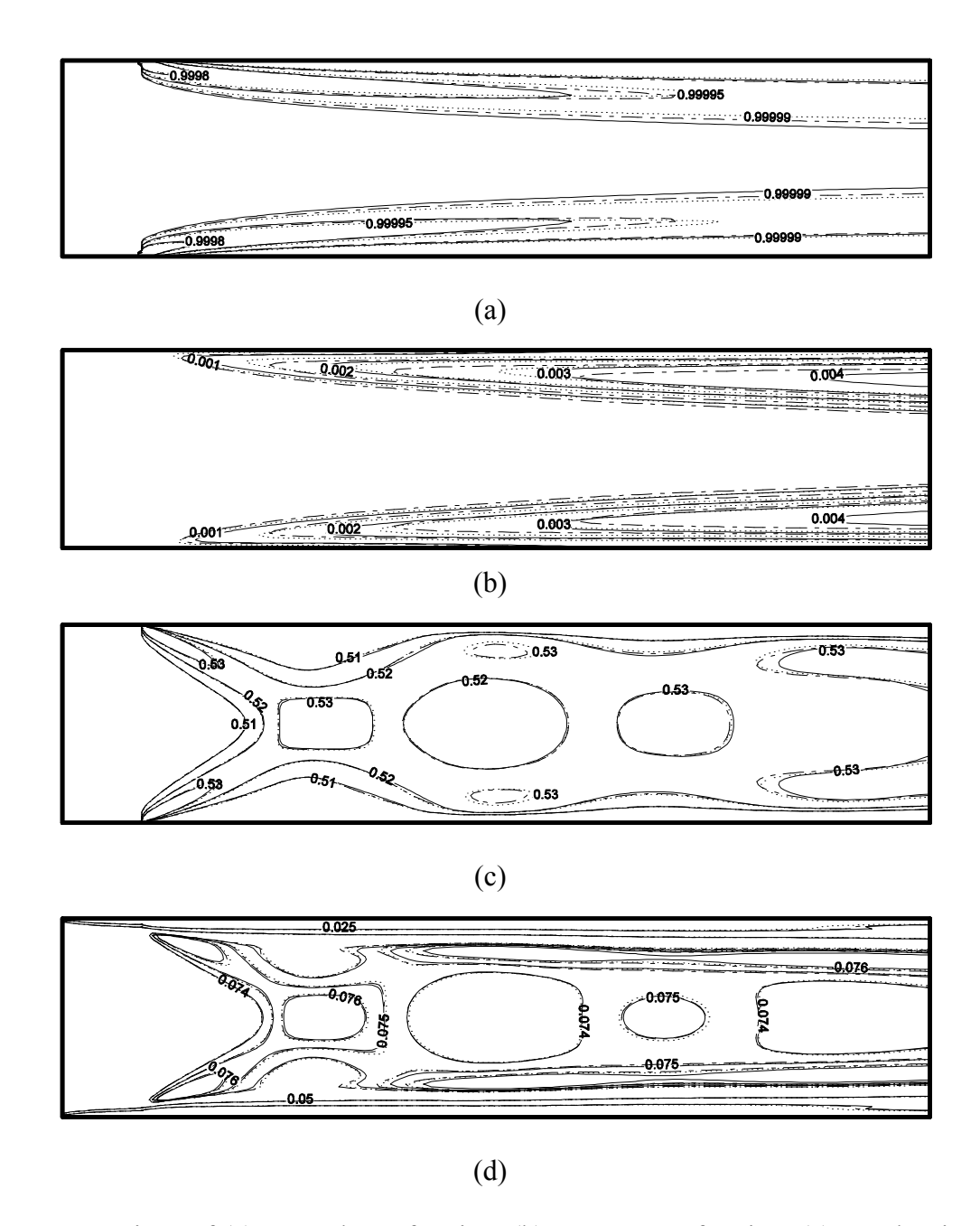
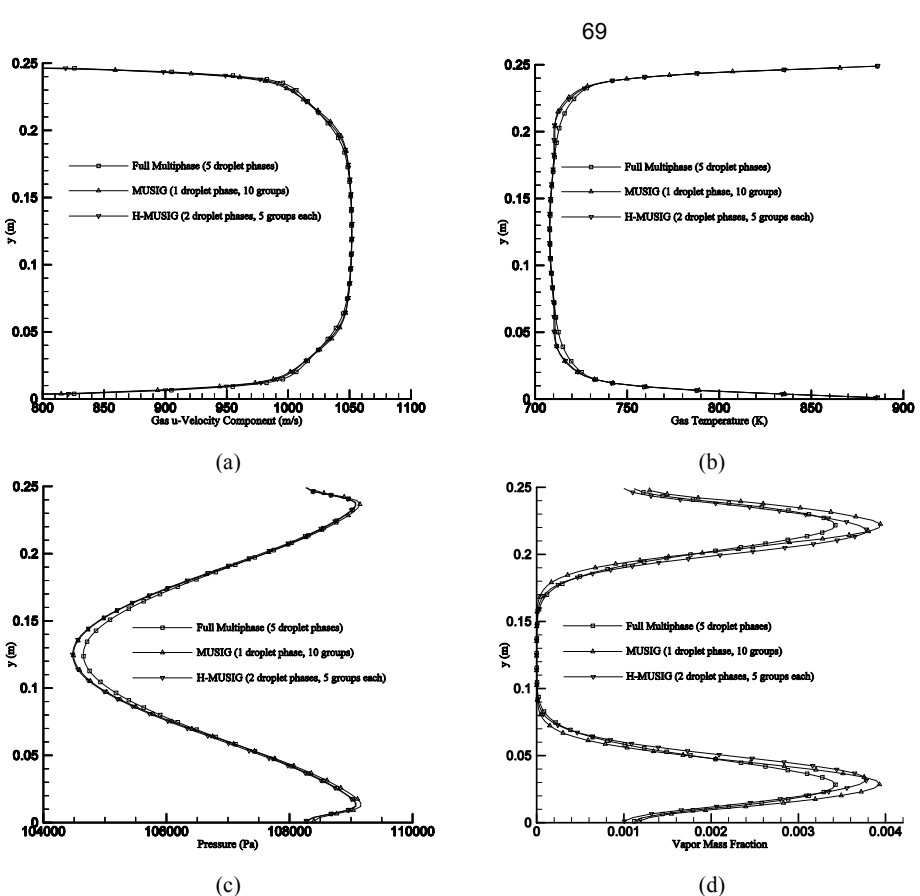
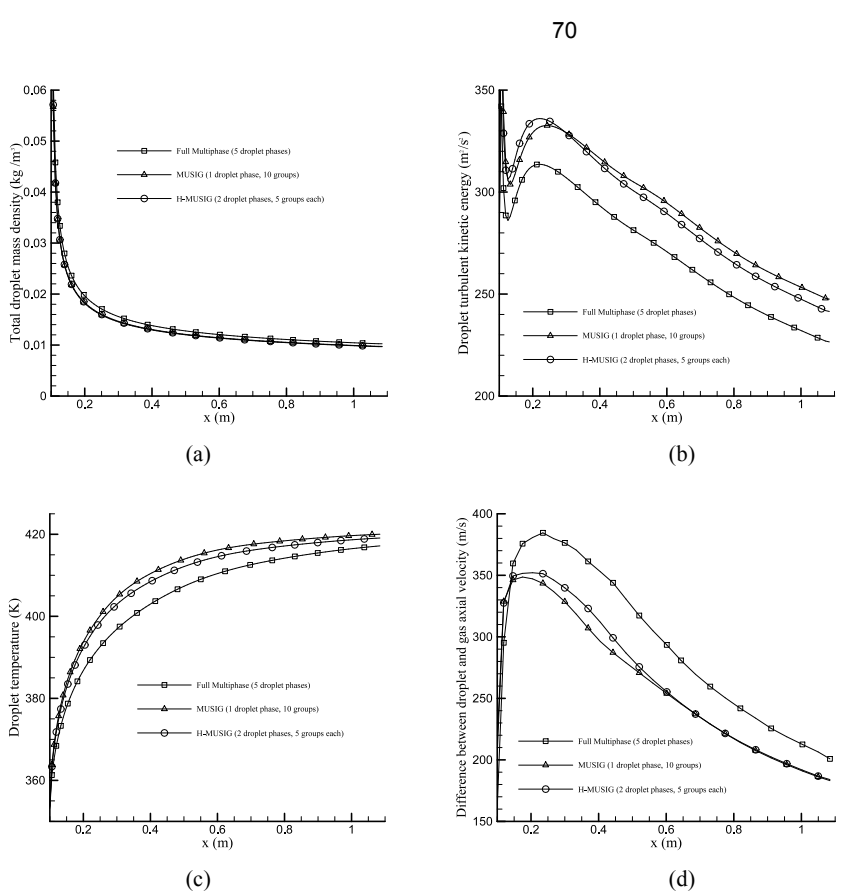


Figure 21 Comparison of (a) gas volume fraction, (b) vapor mass fraction, (c) gas density, and (d) gas turbulent viscosity contours generated using the Full multiphase method with 5 droplet phases (solid line), the H-MUSIG method with 2 droplet phases and 5 size groups per phase (dashed lines), and the MUSIG method with 10 size groups (dotted lines) ( $M_{in}$ =2, cross stream injection).



(c) (d) Figure 22 Comparison of (a) u-velocity, (b) temperature, (c) pressure, and (d) vapor mass fraction profiles across the domain at x=0.6m generated using the full multi-phase, MUSIG, and H-MUSIG methods ( $M_{in}=2$ , cross stream injection).



(c) (d) Figure 23 Comparison of the average droplet (a) mass density, (b) turbulent kinetic energy, (c) temperature, and (d) relative axial velocity in the streamwise direction generated using the full multi-phase, MUSIG, and H-MUSIG methods ( $M_{in}$ =2, cross stream injection).